IGC NEWSLETTER

ISSN 0972-5741, Volume 148, Issue 3 (April-June), July 2026

Director's Message

- First Criticality of PFBR
- Hydrogen Production Facility using Nuclear Heat from FBTR

Research Scholar's Forum

- Development of Non-Destructive Methodology for Identification of Deformation Strain

IGCAR Lecture Series

- Development of Two-Phase Flow and Heat Transfer Models for Corium Transport after a Severe Accident in a Sodium Cooled Fast Breeder Reactor
- Pyrochemical Reprocessing: Principles, Process and Perspectives
- Non-destructive Assay of Actinides using In-house Established Hybrid-KED/Calorimetry Techniques
- Role of Electron Microscopy to Study Irradiation Effects in Materials
- Design and Development of Sensors for Sodium Systems
- Quality Assurance Challenges during Mechanical Construction of FBR Projects
- Chemistry of Cold-Isolated Molecules
- Irradiation of Reactor Materials in Fast Breeder Test Reactor (FBTR)
- Residual Risk in Nuclear Safety: Towards a Concept of Inherent Core Damage Frequency
- Process & Instrumentation for Metal Fuel Fabrication

News and Events

Awards, Honours and Recognitions

Bio-diversity @ DAE Campus, Kalpakkam

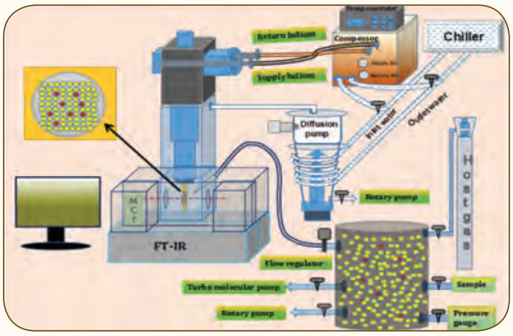

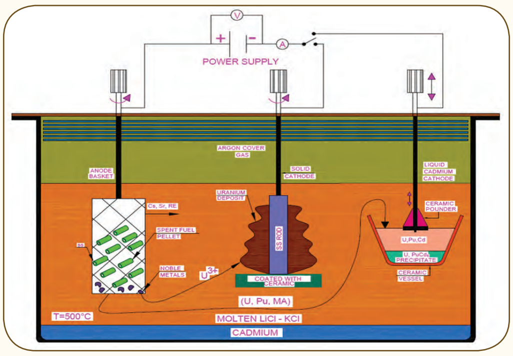

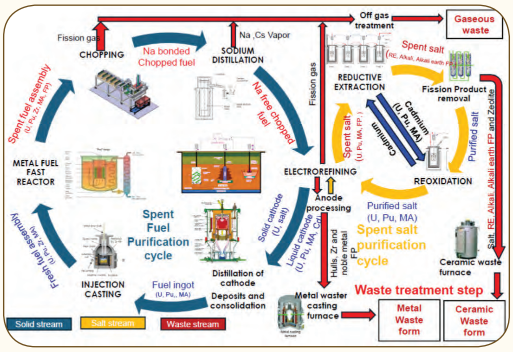

Indira Gandhi Centre for Atomic Research
http://www.igcar.gov.in/lis/nl148/igc148.pdf

Editor's Desk

Dear Reader,

Greetings

It is my privilege to present the latest issue of IGC Newsletter (Volume 148, Issue 3, July 2026). I thank my team for their timely inputs, cooperation, and support in bringing out this issue.

The IGCAR Lecture Series articles on "Development of Two-Phase Flow and Heat Transfer Models for Corium Transport after a Severe Accident in a Sodium Cooled Fast Breeder Reactor" by Dr. Ram Kumar Maity; "Pyrochemical Reprocessing: Principles, Process and Perspectives" by Shri Sourabh Agarwal; "Non-destructive Assay of Actinides using In-house Established Hybrid-KED/Calorimetry Techniques" by Dr. M. Bootharajan; "Role of Electron Microscopy to Study Irradiation Effects in Materials" by Dr. S. Amirthapandian; "Design and Development of Sensors for Sodium Systems" by Dr. Prashant Sharma; "Quality Assurance Challenges during Mechanical Construction of FBR Projects" by Shri G. Ramesh; "Chemistry of Cold-Isolated Molecules" by Dr. N. Ramanathan; "Irradiation of Reactor Materials in Fast Breeder Test Reactor (FBTR)" by Shri Pramod Kumar Chaurasia; "Residual Risk in Nuclear Safety: Towards a Concept of Inherent Core Damage Frequency" by Dr. Pramod Kumar Sharma and "Process & Instrumentation for Metal Fuel Fabrication" by Shri G. Yathish Kumar are included in this Newsletter.

The back cover features a Little Egret photographed at the DAE campus, Kalpakkam.

The Editorial Committee would like to thank all the contributors. We look forward to receiving constructive suggestions from readers towards improving the IGC Newsletter content.

We express our deepest gratitude to the Director, IGCAR, for his keen interest and guidance.

With best wishes and regards

Shri J. Rajan
Chairman, Editorial Committee, IGC Newsletter
Head, Scientific Information & Networking Division, IGCAR

Message by Director, IGCAR

Shri Sreekumar G. Pillai
Director, IGCAR

Dear Colleagues,

The attainment of first criticality of the Prototype Fast Breeder Reactor (PFBR) on 6th April, 2026 marks a defining moment and a major milestone in our nuclear power programme. This historic achievement reflects the strong support and encouragement of our Hon'ble Prime Minister, Narendra Modi ji, and the steadfast leadership and guidance of Dr. A.K. Mohanty, Chairman, AEC and Secretary, DAE whose vision and leadership have been instrumental in bringing this complex programme to fruition.

It is also a proud realization of the long-standing vision of Homi Jehangir Bhabha, whose three-stage programme laid the foundation for harnessing our vast thorium resources. This milestone stands on the strong foundation laid by generations of retired scientists and engineers, whose pioneering work continues to guide and inspire us.

The lead role played by IGCAR in design, technology development and integration has been central to this achievement. The seamless translation of design into construction by BHAVINI has been pivotal in realizing PFBR, supported by the collective strength, technical excellence, and perseverance of teams across BARC, NFC and NRB.

As we move forward, PFBR strengthens the second stage of the programme through a closed fuel cycle and opens the pathway towards large-scale utilisation of thorium, reinforcing India's long-term energy security and self-reliance. Looking ahead, this achievement paves the way for accelerated deployment of future Fast Breeder Reactors, strengthening the second stage and advancing towards large-scale utilisation of thorium in the third stage of our programme.

Let us take pride in this achievement and continue our journey with renewed commitment and purpose.

Congratulations to all the colleagues of IGCAR and BHAVINI.

DAE Inaugurates World's First Hydrogen Production Facility based on Copper–Chlorine Thermochemical Cycle using Nuclear Heat from Fast Breeder Test Reactor

- World's first Copper–Chlorine thermochemical hydrogen production facility using nuclear heat from FBTR.
- Built upon the unique capabilities of FBTR, India's only operating fast reactor research facility.
- Demonstrates IGCAR's leadership in advanced reactor technologies and innovative non-electric applications of nuclear energy.
- Showcases the successful translation of BARC's indigenously developed Copper–Chlorine thermochemical hydrogen production technology.
- Advances India's three-stage nuclear programme by expanding the role of nuclear energy beyond electricity generation into clean hydrogen production.

Director, IGCAR stated, "This achievement builds upon more than four decades of operational experience and technological excellence gained through the Fast Breeder Test Reactor programme at IGCAR. The successful demonstration of hydrogen production using nuclear process heat showcases the versatility of advanced nuclear systems and underscores IGCAR's commitment to developing innovative technologies that contribute to India's clean energy transition and long-term energy security."

Dr. S Lavanya, completed her B.Tech in Metallurgical and Material Science Engineering from Rajiv Gandhi University of Knowledge Technologies (RGUKT), RK Valley, Kadapa in 2015. She joined Indira Gandhi Centre for Atomic Research (IGCAR), Kalpakkam in 2015 to pursue her integrated PhD (dual degree) under Homi Bhabha National Institute. Her research focused extensively on characterizing the deformation and phase transformation induced residual stress (RS) development in ferritic (HSLA) steel and austenitic stainless steel of type 304L by non-destructive methods during tensile, press-brake and roll bending deformations. She also worked at JSW Steel Ltd. Vijayanagar Works, where she focused on the development of advanced hot-dip galvanized coatings, leading research from laboratory studies to industrial trials for large-scale production. She has published four research articles in peer-reviewed international journals.

RESEARCH SCHOLAR'S FORUM

Development of Non-Destructive Methodology for Identification of Deformation Strain

According to Newton's Third Law, "*every action has an equal and opposite reaction*," elastic Residual Stress (RS) develops and remains within the material under equilibrium conditions after deformation, generated during manufacturing processes. The locked-in RS contributes to the applied stress during service and may lead to component failure. The concept of RS has historical relevance in the failure of the famous Silver Bridge (an eye-bar suspension bridge on the Ohio River), which collapsed in 1967 due to Stress-Corrosion Cracking (SCC) in one of its eye bars. A summary of RS-related failure analysis indicates that the majority of cases in steel are due to SCC and joining-related failures.

Type 304L Austenitic Stainless Steel (ASS) is widely used in critical components in the nuclear industry, including containment vessels, piping, storage systems, and structural elements, due to its excellent balance of corrosion resistance, mechanical strength, and weldability. It is well known that SS 304L undergoes a Strain-Induced Martensitic (SIM) transformation during plastic deformation below the M_d temperature (the temperature at which martensite formation starts during deformation). While the mechanical properties are dependent on the phase fractions, the resultant RS is the synergistic effect of plastic deformation and phase transformation in SS 304L. Hence, knowledge of RS is crucial for understanding the deformation behaviour of SS 304L, which is a prime factor in the performance assessment of manufactured components. The interplay between mechanical deformation, phase evolution, and the resulting RS state is influenced by factors such as material composition, processing conditions, and temperature. While significant progress has been made in characterising the deformation-induced RS, several challenges remain in understanding the coupled effects of deformation and phase transformation on RS evolution. Additionally, the need for online monitoring of a process is increasing, as assessing structural integrity is essential for predicting and preventing catastrophic failures. In view of this, the present work aims to develop a non-destructive methodology to identify deformation strain from RS analysis.

In this study, the evolution of RS during tensile deformation of metastable SS 304L (3 mm thick sheet) and after fracture is analysed. The RS that arises after sheet metal forming processes, such as press brake and roll bending, is analyzed based on results from tensile tests. Towards this objective, tensile deformation was carried out at different strain rates ($\dot{\varepsilon}$) in the quasi-static regime at RT and 200 °C (where SIM transformation is prevented). In addition, interrupted tensile tests were performed to understand the evolution of RS with strain at two different $\dot{\varepsilon}$ at RT for strains ranging from the material Yield Strength (YS) to Ultimate Tensile Strength (UTS). Similarly, press brake bending was carried out to different bend angles and roll bending to different diameters. Table 1 presents the test matrix used in the present study. RS was measured on the deformed sample surface using X-ray diffraction (XRD) based on the $\mathrm{Sin}^2\psi$ technique with the Proto-iXRD instrument. The macro RS/strain (averages over several grains) is measured from the XRD peak shift and the micro-strain from XRD peak broadening. In case of tensile deformation, longitudinal RS (RS along the tensile deformation axis) and transverse RS (perpendicular to the tensile axis) are measured in the gauge region of the austenite and α'-martensite phase at various interrupted strains and fractured samples.

Table 1: Test matrix of experiments carried out in the present study

Tensile deformation				
Tests	Temperature	Interrupted strains at room temperature		Strain rate ($\dot{\varepsilon}$) s^{-1}
Tensile tests	Room temperature (25 °C)	$5.21 \times 10^{-4}\ s^{-1}$	0.033, 0.14 0.31, 0.47 0.63, 0.72	5.21×10^{-4} 2.1×10^{-3} 5.21×10^{-3} 1.3×10^{-2} 2.6×10^{-2}
	200 °C	$1.3 \times 10^{-2}\ s^{-1}$	0.004, 0.09 0.19, 0.33 0.48, 0.54	
Bending deformation				
Press brake bending	Room temperature	Bend angles: 45°, 60°, 90°, 108°, 120°, 135°		
Roll bending	Room temperature	Bend diameter: 400 mm, 600 mm, 800 mm, 1000 mm		

The formation of SIM during RT deformation and its volume fraction are estimated from XRD-based retained austenite (RA) analysis. The XRD patterns of specimens deformed to various tensile strains for a $\dot{\varepsilon}$ of $5.21 \times 10^{-4}\ s^{-1}$ are shown in Fig. 1a, which confirms the evolution of BCC α'-martensite (SIM) phase. The variation of α'-martensite fraction with strain and $\dot{\varepsilon}$ are presented in Figs. 1b and 1c respectively. It is observed that a significant increase in α'-martensite fraction is noticed after a particular strain of 0.33 irrespective of $\dot{\varepsilon}$ variation. However, the volume fraction is observed to decrease with an increase in strain rate (Fig. 1c).

To understand the variation in RS with strain, the average longitudinal and transverse RS in the gauge region of the austenite and α'-martensite is considered. The RS variation with strain is shown in Fig. 2. Fig. 2a presents the RS variation in the austenite phase. The longitudinal RS (solid symbols) in austenite is observed to decrease with an increase in tensile strain, irrespective of variation in $\dot{\varepsilon}$. After tensile deformation, the stresses changed from compressive to tensile stress state (64 ± 11 MPa) when deformed to a strain of 0.004 (strain just above the material YS) at a $\dot{\varepsilon}$ of $1.3 \times 10^{-2}\ s^{-1}$. However, on further straining, deformation-induced RS changes from tensile to compressive at a strain level greater than 0.33. A reduction in RS with tensile strain and $\dot{\varepsilon}$ is attributed to the increased work hardening and associated SIM transformation in SS 304L material, which are in accordance with the observations reported earlier. Fig. 2a also shows the variation in transverse RS (open symbols) of the austenite phase, which increases marginally up to 0.33 strain and decreases upon further deformation. However, the effect of $\dot{\varepsilon}$ was negligible on transverse RS. Similarly, Hedström et al. reported an insignificant change in transverse RS in the austenite phase during the tensile deformation of ASS of type 301 from 0 to 0.05 strain. The variation of RS in the α'-martensite phase with strain in two $\dot{\varepsilon}$ are shown in Fig. 2b. It is observed that the longitudinal RS are in tensile stress state while the transverse RS are in compression. The observed variation of RS between the longitudinal and transverse directions in both the austenite and α'-martensite phases indicates a balance of RS among the phases, as well as along the deformation direction and perpendicular to it. Similar behaviour of the RS balance is also reported by Hedström et al. in 301 ASS in the austenite and martensite phases.

In addition, the evolution of the RS distribution after fracture

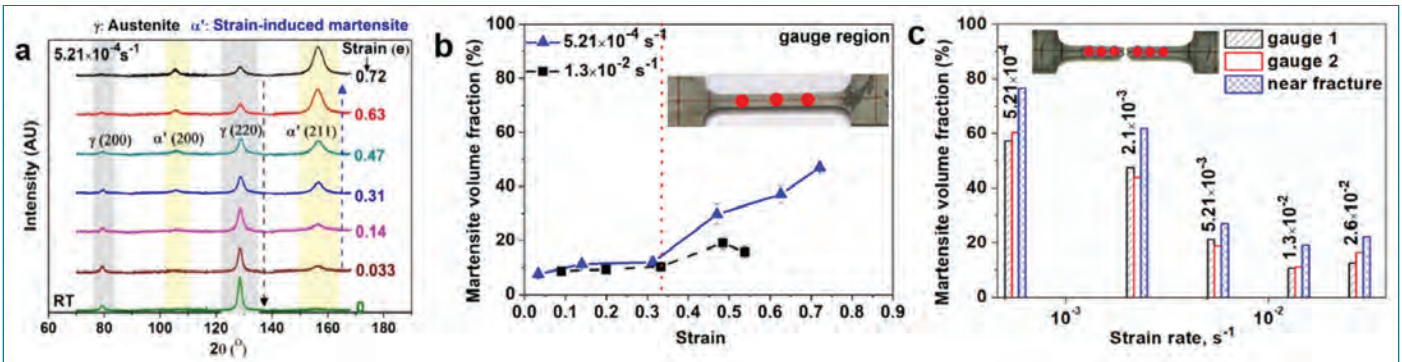

Fig. 1: XRD profile obtained for various a) interrupted strains at a of $5.21 \times 10^{-4}\ s^{-1}$, variation in the α'-martensite volume fraction with b) strain c) strain rate

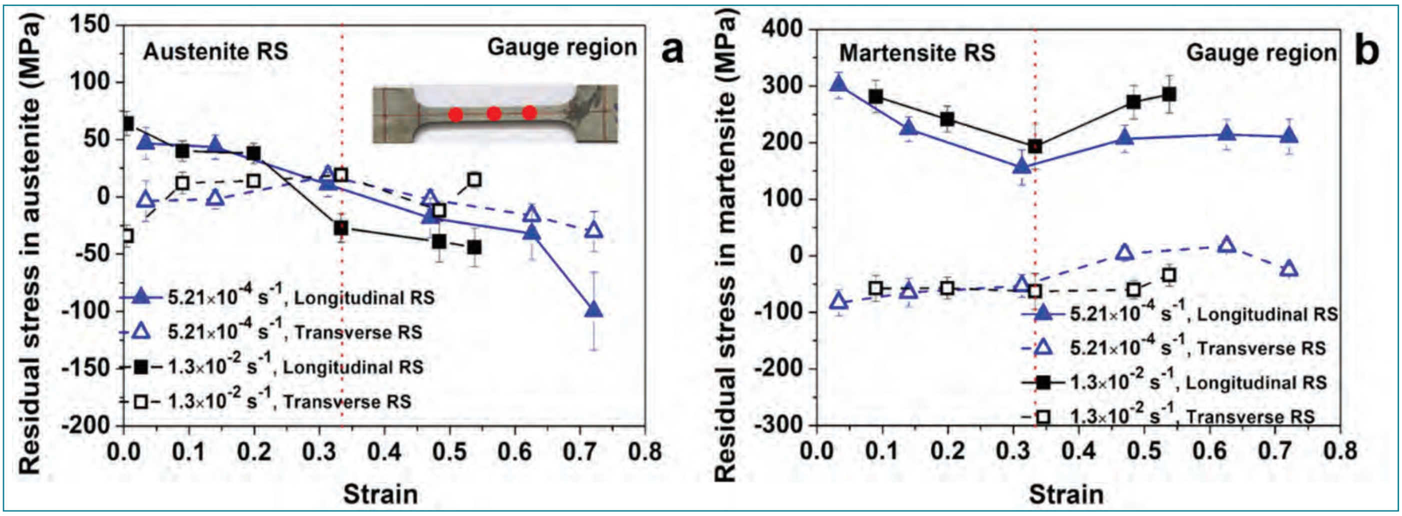

Fig. 2: The RS variation with strain in a) austenite and b) α'-martensite phase

is demonstrated with the RS maps obtained by measuring stress in the austenite phase at multiple locations on the gauge and fracture regions. Fig. 3 presents the RS evolution for a $\dot{\varepsilon}$ of 1.3×10^{-2} s^{-1}. Figs. 3a and 3b show the RS distribution for a sample deformed till YS and UTS, respectively, which clearly indicate the decrease in RS with strain (also shown in Fig. 2a). After fracture (Fig. 3c), it is noticed that the gauge region remains in a compressive stress state with increased magnitudes. However, high tensile RS prevails near the fracture region of the RT tensile fractured sample. Similar distribution of RS is observed in tensile fractured specimen deformed at 200 °C, as can be seen from Fig. 3d. Interestingly, the gauge region of the specimen deformed at 200 °C exhibits tensile RS with maximum being observed near the fracture region. It is observed that the extent of tensile RS affected region is more prominent in the specimens deformed at 200 °C as compared to RT deformation. The high-tensile RS near fracture region in case of both RT and 200 °C deformation is attributed to the triaxial stress state that occurs during necking before failure. The observed lower magnitudes of RS in case of RT deformation than the 200 °C deformation is due to the formation of SIM, which acts as a hard dispersoid in the soft austenite matrix as well as the volume expansion.

It is known that microstrain broadens XRD peaks, and the peak width indicates the amount of plastic strain in the material due to lattice defects. Recent studies have examined the Full Width at Half Maximum (FWHM) of these diffraction peaks, obtained from line profile analysis, to assess the microstrain

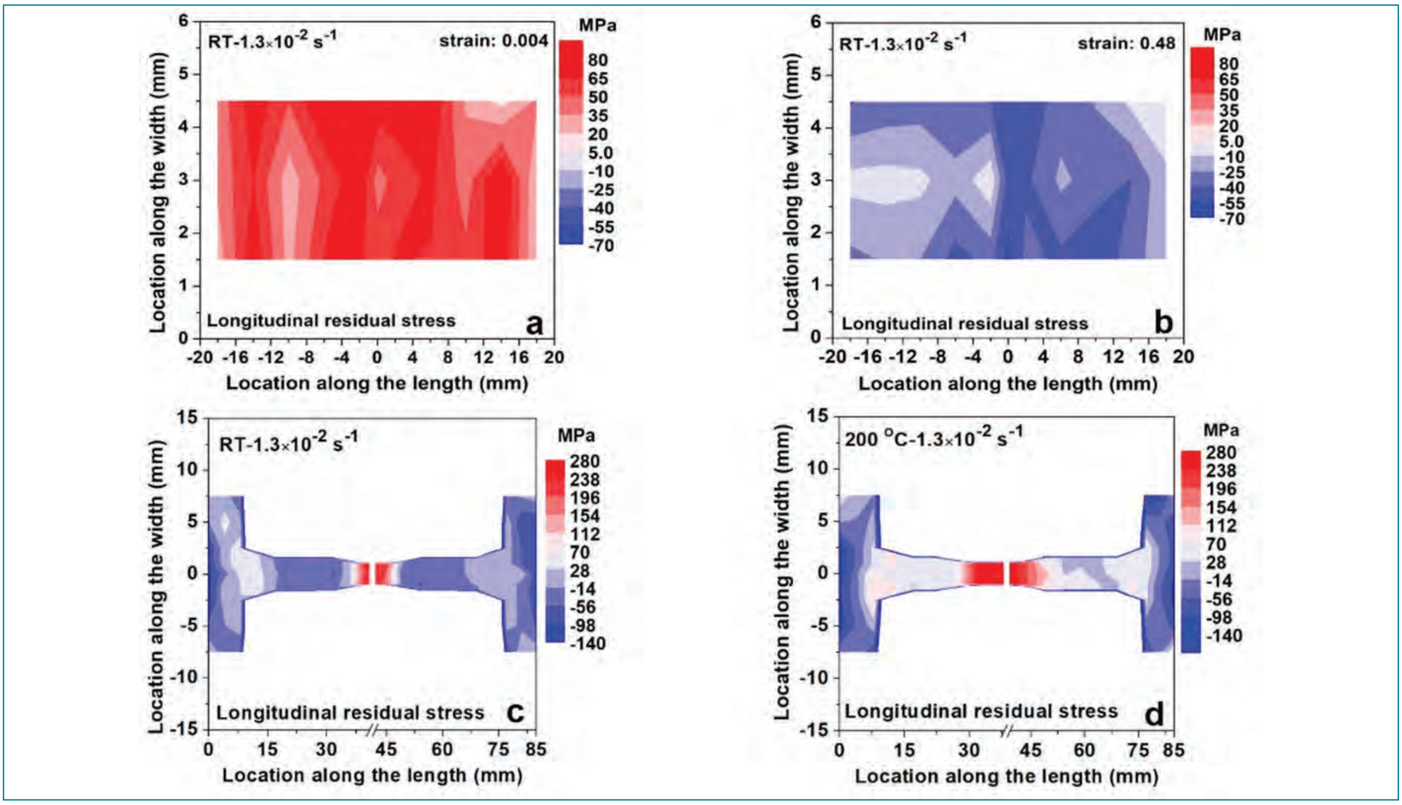

Fig. 3: Austenite phase longitudinal RS distribution in specimens deformed at of 1.3×10^{-2} s^{-1} a) interrupted to a strain of 0.004 (YS), b) interrupted to a strain of 0.48 (UTS), c) after fracture at RT, d) after fracture at 200 °C

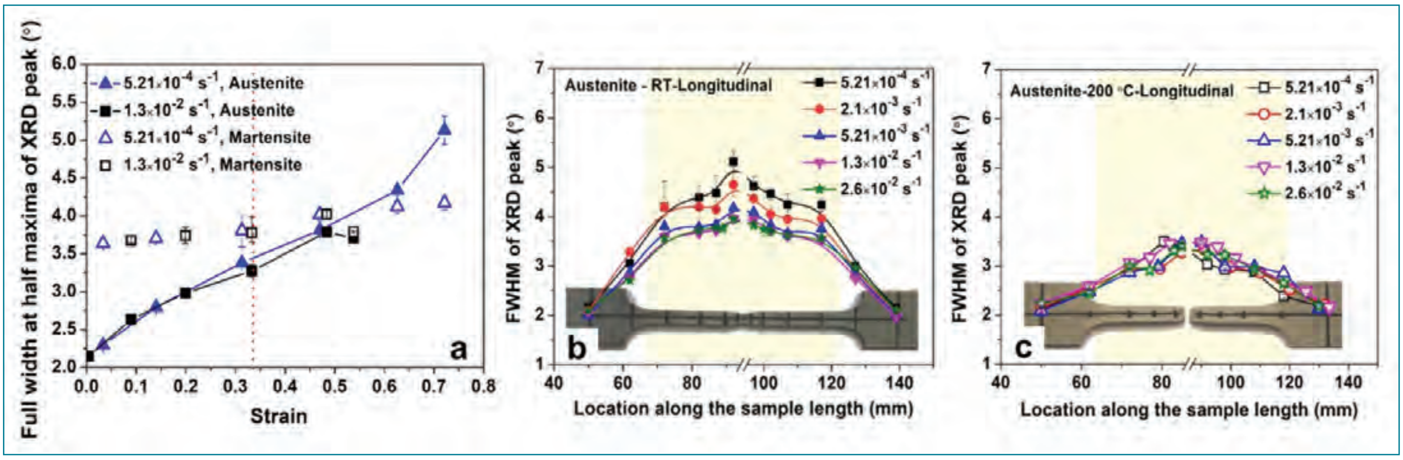

Fig. 4 a) Variation in FWHM of XRD peak with strain at of 5.21×10^{-4} s^{-1} and 1.3×10^{-2} s^{-1} in the austenite and α'-martensite phase. Distribution of FWHM of XRD peak in the austenite phase for varied at b) RT c) 200 °C

variations related to micro RS. In the present study, FWHM of the XRD peaks obtained for each investigated test condition is considered for the analysis. The variation of FWHM of austenite and α'-martensite phase at interrupted tensile strain levels is shown in Fig. 4a. It is observed from Fig. 4a that a continuous increase in FWHM is noticed in the austenite phase, indicating hardening due to the dislocations. However, variations in the FWHM of α'-martensite phase with strain are marginal as compared to those in the austenite phase. These observations are similar to the findings of Talonen, that the variations in dislocation density in the austenite phase are significant, while α'-martensite remained constant even for higher SIM fractions. The effect of $\dot{\varepsilon}$ and temperature on the FWHM of XRD peak corresponding to the austenite phase are shown in Figs. 4b and 4c, respectively. Fig. 4b presents the FWHM variations in the specimens deformed at RT and Fig. 4c shows the variation for deformations at 200 °C. A comparison of the deformation at RT and 200 °C reveals that the deformation at RT shows higher FHWM, which is attributed to the increased microstrain due to plastic deformation and associated α'-martensite transformation. It is known that the α'-martensite introduces additional dislocations into the austenite phase leading to higher microstrain in the austenite phase. The observed higher FWHM in the lower deformations at RT corroborates with the higher plastic deformability and α'-martensite volume fractions (Fig. 1c).

The primary objective of the study is to develop a methodology for non-destructively identifying the unknown deformation strain using the RS analysis. Towards this, changes in longitudinal RS measured in the gauge region of the austenite phase at various interrupted strains (which coincide with the tensile deformation axis) are considered for the analysis. The variation of FWHM of the austenite peak is considered, wherein significant variations are observed as compared to insignificant variations in α'-martensite (Fig. 4a). Fig. 5a shows the variation in RS vs FWHM in the gauge region of austenite phase at different interrupted strains and two $\dot{\varepsilon}$ at RT. The results show a systematic decrease in RS with FWHM of the XRD peak, indicating the influence of plastic deformation. To estimate the deformation level after fracture, RS and FWHM measured in the gauge region of the specimens fractured at these two $\dot{\varepsilon}$ are superimposed (on Fig. 5a) and shown as open symbols in Fig. 5b. It is evident that

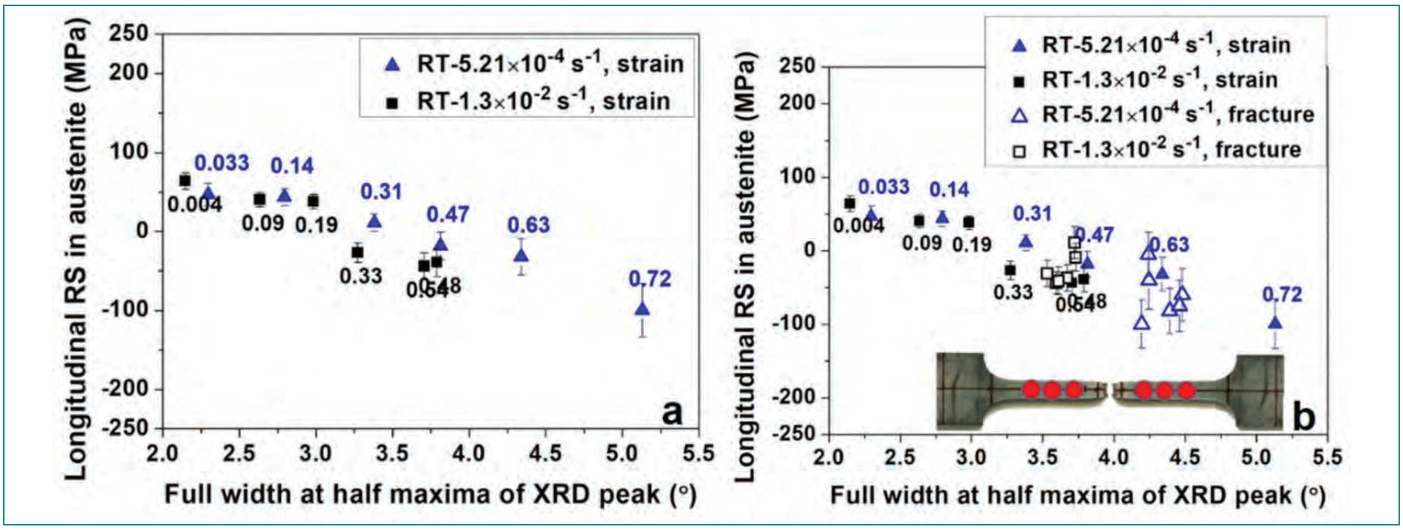

Fig. 5: RS vs FWHM of austenite phase for RT deformation at two $\dot{\varepsilon}$ for a) interrupted strains (legend strain indicate interrupted strains) b) after fracture

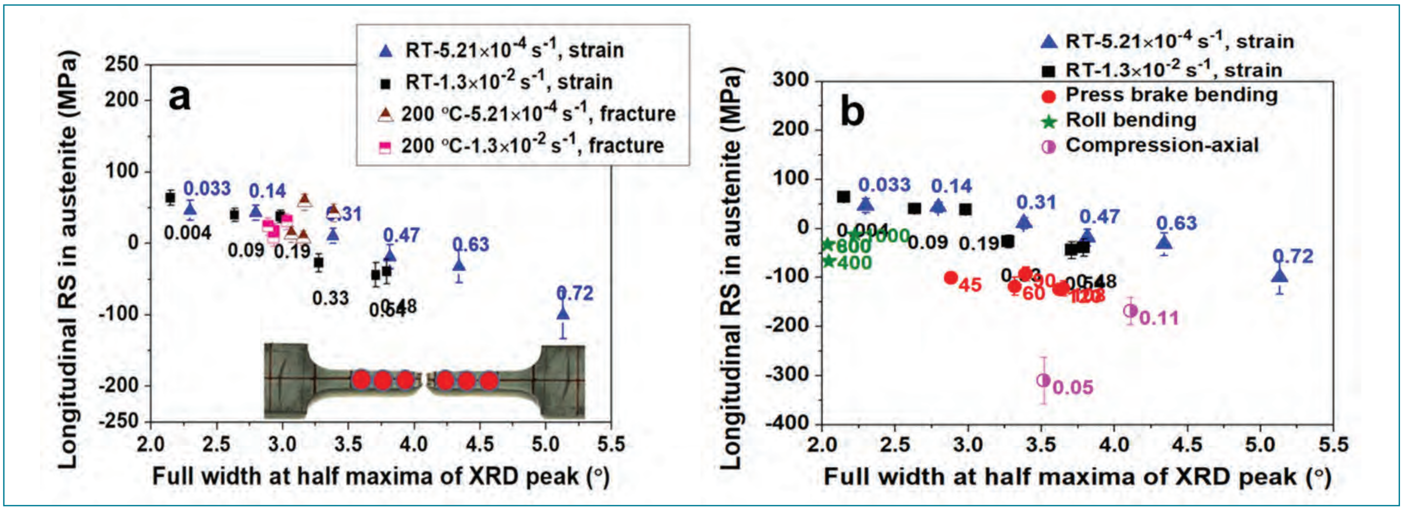

Fig. 6 a) RS vs FWHM of austenite phase for 200 °C deformations after fracture at two $\dot{\varepsilon}$ incorporating with interrupted strain data b) incorporating the RS vs FWHM of the press brake, roll bending and uni-axial compression data

the measured RS and FWHM values in the gauge region of fractured specimens lie within the band of interrupted strain data of respective $\dot{\varepsilon}$ deformations. The RS and FWHM values of fractured specimens deformed at a lower $\dot{\varepsilon}$ (5.21×10^{-4} s^{-1}) lie close to a strain level of 0.63, whereas the specimen deformed at a higher $\dot{\varepsilon}$ (1.3×10^{-2} s^{-1}) lies between 0.48 and 0.54 strains. These strain levels are indicative of near UTS deformation.

Further, the analysis of RS and FWHM variations after fracture has been extended to specimens tensile deformed at 200 °C for two $\dot{\varepsilon}$ ($\dot{\varepsilon}$ used at RT). The variation of longitudinal RS and FWHM in the austenite phase incorporating the deformation at 200 °C data is shown in Fig. 6a. Interestingly, the RS and FWHM data lie within the interrupted tensile strains encountered at RT. The deformation strain (corresponding to elongation) at 200 °C is smaller than the deformation strain at RT for the respective $\dot{\varepsilon}$. These observations of RS and FWHM variations in the gauge region of tensile fractured specimens (at RT and 200 °C) indicate that the deformation strain in these regions can be estimated from RS and FWHM plots obtained at different interrupted strain levels and $\dot{\varepsilon}$.

To extend the utility of the above approach for estimating deformation in other forms, data from press-brake bending and roll bending were considered. The different bending angles and roll bend diameters studied represent the different levels of deformation. In both cases, the RS and FWHM of the austenite phase on the outside surface of the bend are considered, as this surface experiences tensile deformation. In press brake bending, the RS measured across the bending line was taken as the location of maximum deformation. For roll bending deformation, the RS measured along the hoop direction at the outside diameter is considered. The observed variations in RS and FWHM of the XRD peak for different bend angles (circle symbols) and roll bend diameters (star symbols) are shown in Fig. 6b, with the legends indicating the respective bend angle and diameter. The press brake bending data lie within the range of 0.14 to 0.47 of tensile strain and increase with bend angle (45° to 120°), consistent with the increased level of plastic deformation required to bend to higher angles. However, the samples rolled to different bend diameters exhibit very low FWHM values, corresponding to very low tensile strains, which align with the deformation levels observed during roll bending. The strains obtained from various roll-bent samples lie just above the material's YS. These observations also confirm that the plastic deformation during press brake bending is higher than that during roll bending.

It is observed that the RS data of press brake bent and roll bent samples are lower in magnitude as compared to tensile deformation, which could be due to the effect of constrained deformation (tension and compression) that occurs during bending. To confirm this behaviour, uniaxial compression of SS 304L was performed at 0.001 $\dot{\varepsilon}$ to two strains, 0.05 and 0.11. The RS measured in the direction of compression (axial RS) is also shown in Fig. 6b. The results show that higher compressive RS are observed in the sample deformed to 0.05 strain than in 0.11 strain, which could be due to the higher elastic recovery in the case of lower compression ratios.

From these findings, it is concluded that a combined analysis of RS and FWHM of XRD peak obtained from XRD measurements could be used as a tool to assess an unknown sample's previous deformation condition. This approach allows for qualitative assessment of RS and deformation level without causing damage to the sample, aiding in understanding the RS variation, preventing abrupt failures, and facilitating failure analysis. It is also emphasised that the data shown here are for the uniaxial tension and compression deformation, and further studies are required to extrapolate these observations to cyclic/fatigue loading.

Dr. RAM KUMAR MAITY
Reactor Design Group
Indira Gandhi Centre for Atomic Research
Kalpakkam, Tamil Nadu, India

LECTURE SERIES

Development of Two-Phase Flow and Heat Transfer Models for Corium Transport after a Severe Accident in a Sodium Cooled Fast Breeder Reactor

1. Background and Motivation

Fast breeder reactors represent a critical component of India's three-stage nuclear power program, operating with compact cores and high-power densities (400-500 kW/litre). While these reactors benefit from large thermal inertia in pool-type configurations, understanding severe accident scenarios—specifically Core Disruptive Accidents (CDA)—remains essential for comprehensive safety analysis. During CDA, core materials may melt and relocate, necessitating accurate prediction of molten fuel and other core structural materials (corium) behaviour as they interact with the liquid sodium coolant (Fig. 1). The transport of corium in sodium involves complex multi-phase phenomena, including two-phase flow dynamics, jet break-up and droplet formation, phase change in both corium (solidification/remelting) and sodium (boiling/condensation), and potential species segregation. Two-phase flow physics itself is a complex and active field of research. Corium transport involves large density ratios, strong surface tension forces, and the development of intricate structures due to two-phase flow instabilities.

While commercial computational fluid dynamics software offer flexibility through unstructured grids, such tools may not always implement state-of-the-art algorithms for challenging two-phase flow problems. The significant density ratios, large surface tension forces, and intricate interface structures encountered in corium-sodium interactions demand highly accurate and robust numerical methods. The development of specialized in-house codes offers several advantages viz. implementation of cutting-edge algorithms optimized for specific physics, reduced computational requirements through efficient algorithmic choices, and detailed control over numerical schemes. Although open-source alternatives are valuable, they typically necessitate extensive validation, may lack implementation of specific physics relevant to the problem, and can exhibit undocumented issues, leading to substantial additional development effort.

In this context, the present work describes the development and application of THYC-MP, an indigenous, in-house developed multi-phase flow solver aimed at high-fidelity simulation of corium–sodium interactions under severe accident conditions. The code is based on a Volume of Fluid

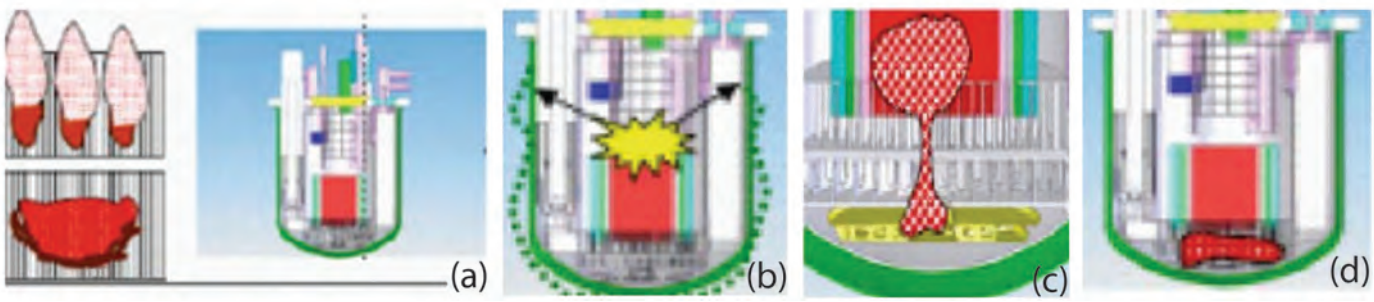

Fig. 1: Phases of a severe accident in a fast reactor—(a) Core melting, (b) Mechanical energy release, (c) Molten fuel relocation, (d) post-accident heat removal (courtesy: J. Rouault et al., "Severe Accidents," in Handbook of Nuclear Engineering, vol. 5, D.G. Cacuci, Ed. New York, NY, USA: Springer, 2010, pp. 2651–2661)

(VOF) framework implemented on structured, non-uniform grids in two-dimensional and axisymmetric domains, with ongoing extensions to three-dimensional configurations and phase change physics. It is capable of capturing complex interface dynamics even on relatively coarser grids, owing to the employment of higher-order numerical methods.

THYC-MP is an indigenous, in-house developed general-purpose multi-phase flow solver, which provides flexibility due to complete access to the source code. This enables incorporation of any new problem-specific physics and advanced numerical algorithms. The framework incorporates state-of-the-art interface reconstruction and curvature evaluation techniques, many of which have been developed as part of this work, and can further serve as a test bed for continued development and evaluation of advanced algorithms across various aspects of two-phase flow. This approach allows continued development toward accurate mechanistic prediction of corium transport phenomena and improved safety analysis of fast breeder reactors.

Two-Phase Flow Solver (THYC-MP)

The complete two-phase flow solver employs a force-balanced pressure–velocity coupling on a fully staggered grid, based on the PROST (Parabolic Reconstruction of Surface Tension) methodology of Renardy and Renardy (2002). The governing equations are formulated implicitly for the momentum predictor step as:

$$\rho\frac{u^{*}-u^{n}}{\Delta t}=-\nabla.(\rho\vec{u}^{n}u^{*})+\frac{\partial}{\partial x}\left(2\mu\frac{\partial u^{*}}{\partial x}\right)+\frac{\partial}{\partial y}\left(\mu\left(\frac{\partial u^{*}}{\partial y}+\frac{\partial v^{n}}{\partial x}\right)\right)+\rho g_x+F_{ST_x}-\frac{\partial P_1}{\partial x}$$

$$\rho\frac{v^{*}-u^{n}}{\Delta t}=-\nabla.(\rho\vec{u}^{n}v^{*})+\frac{\partial}{\partial y}\left(2\mu\frac{\partial v^{*}}{\partial y}\right)+\frac{\partial}{\partial x}\left(\mu\left(\frac{\partial u^{n}}{\partial y}+\frac{\partial v^{*}}{\partial x}\right)\right)+\rho g_y+F_{ST_y}-\frac{\partial P_1}{\partial y}$$

The pressure correction is obtained from:

$$\nabla.\left(\frac{\nabla P_2}{\rho}\right)=\nabla.\frac{\vec{u}^{*}}{\Delta t}$$

followed by the velocity update:

$$\frac{\rho}{\Delta t}(u^{n+1}-u^{*})=-\frac{\partial P_2}{\partial x},\frac{\rho}{\Delta t}(v^{n+1}-v^{*})=-\frac{\partial P_2}{\partial y}$$

A key feature of the formulation is the force-balanced treatment of surface tension. A capillary component of pressure is explicitly defined that balances the surface tension force, with total pressure being: $P=P_1+P_2$.

$$\nabla\cdot\mathbf{F}_{ST}=\nabla\cdot\nabla P_1$$

This ensures that the surface tension force is exactly balanced by the gradient of capillary pressure (∇P_1), thereby satisfying the Laplace equilibrium and eliminating spurious currents. The solver is implemented on a fully staggered grid, with pressure and volume fraction stored at cell centers, u-velocity at vertical cell faces, and v-velocity at horizontal cell faces.

Two-phase modelling involves the representation and numerical simulation of the simultaneous flow of two distinct phases with dynamically evolving interfaces. The governing framework is based on the Navier–Stokes equations, with requirement of additional terms to account for interfacial forces such as surface tension, along with appropriate closure models. Methods for modelling two-phase flows can be broadly classified into moving grid and fixed grid approaches. Fixed grid methods are generally simpler and more efficient to implement, as they avoid the need for re-meshing and the associated interpolation errors inherent to moving grid techniques. Within fixed grid frameworks, further classification is possible into front tracking and front capturing methods, depending on whether discrete marker particles or continuous marker functions are used to represent the interface between phases. Among front capturing approaches, the Volume of Fluid (VOF) method is particularly attractive due to its ability to accurately conserve the mass of each phase while handling large interface deformations. Accurate modelling of two-phase systems is particularly challenging due to large density and viscosity contrasts, complex interface topologies and phase change phenomena. Consequently, the development of robust and high-fidelity numerical methods remains an active area of research, especially for applications involving interfacial instabilities, breakup, coalescence, and transport processes.

2. Volume of Fluid (VOF) Method Framework

The Volume of Fluid method serves as the foundation for the present work, offering superior mass conservation compared to level-set approaches. In VOF, each computational cell contains a volume fraction representing the primary phase:

$$f=1: cell\ completely\ filled\ with\ primary\ phase$$

$$0<f<1: mixed\ cell\ containing\ both\ phases$$

$$f=0: cell\ completely\ filled\ with\ secondary\ phase$$

The volume fraction evolves according to the advection equation:

$$\partial f/\partial t + u\cdot\nabla f = 0$$

The primary steps in a VOF-based two-phase flow solver are illustrated in Fig. 2. These include interface reconstruction from the volume fraction field, interface advection via the volume fraction conservation equation, evaluation of surface tension forces, their incorporation into the Navier–Stokes equations, and subsequent solution of the flow field. Key contributions to each of these steps are outlined in the following sections.

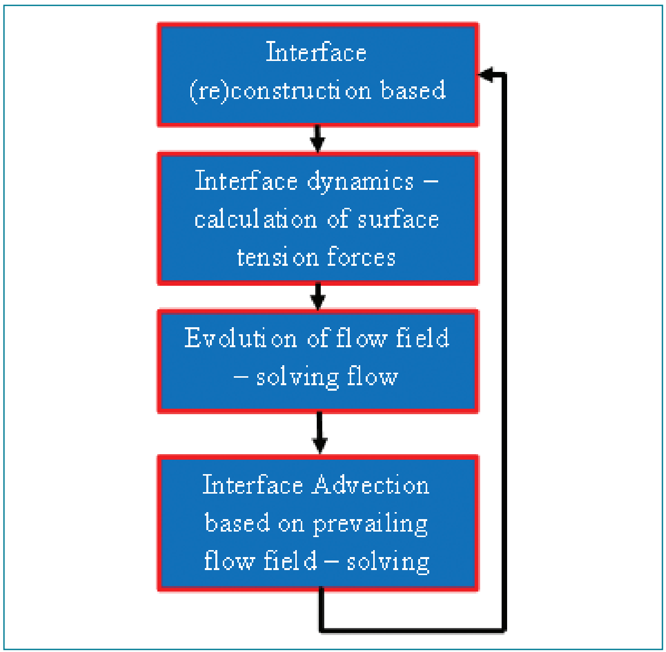

Fig. 2: Flow chart of the main steps in a VOF based two phase flow solver

3. Interface Reconstruction: The PCIC Method

A novel Piecewise Circular Interface Construction (PCIC) method was developed to achieve higher-order accuracy in interface reconstruction. In this approach, interfaces are represented as circular arcs rather than linear segments, improving static reconstruction accuracy. The method demonstrates near third-order convergence with grid refinement. In addition, the use of cell-wise circular arcs enables smoother interface representation by more accurately capturing local curvature. The PCIC method operates in two stages. The first stage, termed Bare PCIC, constructs circular arcs by fitting points obtained from PLIC interfaces over a nine-point stencil. PLIC stands for Piecewise Linear Interface Construction, in which appropriately oriented line segments are used to represent cell-wise interfaces. The second stage introduces a C^0 correction, enforcing continuity at cell boundaries and significantly reducing reconstruction errors. A family of hybrid variants (H1-PCIC and H2-PCIC) has also been developed, combining PCIC-based interface geometry with curvature evaluation from the Height Function method. Static interface reconstruction tests on ellipses, with a maximum-to-minimum curvature ratio of 14.697, demonstrate substantial improvements. A representative result for reconstruction error of randomly generated ellipses on a 320×320 grid is presented in Table 1.

Table 1: Error of reconstruction of 100 random ellipses on a 320 × 320 grid (ELVIRA stands for Efficient Least-squares Volume-of-fluid Interface Reconstruction Algorithm)

Method	Grid Size	Error	Order of Convergence
Young's PLIC	320×320	2.49E-06	~2.0
ELVIRA	320×320	2.07E-06	~2.0
PCIC (bare)	320×320	1.78E-06	2.94
PCIC (c0)	320×320	5.41E-07	2.95

For complex shapes, PCIC(c0) maintains nearly third-order accuracy even on coarse grids, outperforming existing higher-order methods.

4. Interface Advection (Volume Fraction Transport): Edge-Matched Flux Polygon Algorithm (EMFPA)

Accurate interface advection requires non-diffusive algorithms that preserve sharp interfaces while ensuring strict mass conservation. The Edge-Matched Flux Polygon Algorithm (EMFPA) achieves these objectives by constructing geometric flux polygons without overlaps or gaps between adjacent cells, thereby enabling exact mass balance and consistent multi-dimensional advection. In the present work, fast analytical procedures have been developed for determining flux polygon vertices, replacing computationally expensive numerical approaches. The analytically derived geometric relations are omitted here for brevity. Dynamic validation is performed using the vortex-in-a-box problem, in which a time-reversible velocity field stretches and deforms an initially circular interface before returning it to its original configuration. This stringent test simultaneously exposes reconstruction and advection errors. The flow is defined through the stream function $\Psi = -\frac{1}{\pi}\sin^2(\pi x)\sin^2(\pi y)\cos\left(\frac{\pi t}{T}\right)$; for $T = 2$, the interface undergoes maximum deformation at before recovering at $t = 2$. The error is defined as the integral of absolute difference between the initial and the final volume fraction fields (L^1 error). Errors from the present work are compared against results from other important published methods with a sample

Table 2: Comparison of errors during vortex in a box test after one complete period (T = 2) (H2-PCIC(c0) is a hybrid variant after combining Height Function calculations with PCIC(c0))

Method	Grid Size	Error	Order of Convergence
LVIRA + EMFPA*	128 × 128	5.62E-05	~2.0
SIR + EMFPA*	128 × 128	4.33E-05	~2.0
PCIC(c0) + EMFPA	128 × 128	4.17E-05	~2.8
H2-PCIC(c0) + EMFPA	128 × 128	3.36E-05	~2.4
*Literature values for comparison			

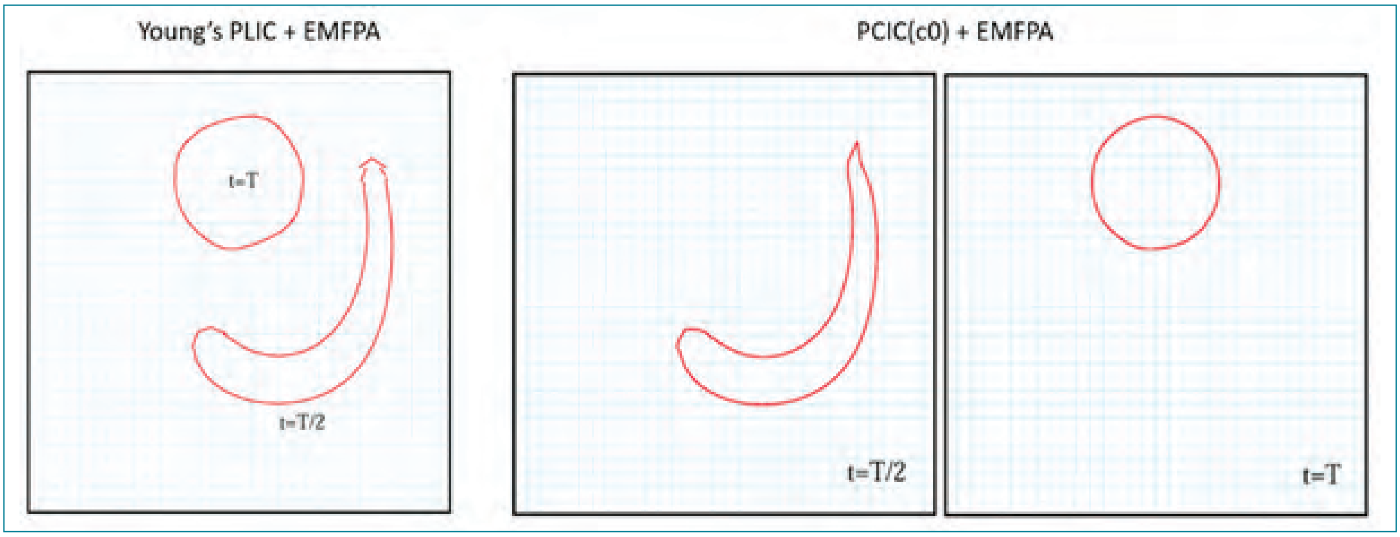

Fig. 3: Visualization of performance of interface reconstruction and two-phase advection modules. Initial interface is a circle centered at x = 0.75, y = 0.5) that gets deformed by a clockwise vortex upto T/2 with subsequently reversing direction. The difference between the configurations at t = 0 and t = T gives the error

result shown in Table 2. The combination of PCIC(c0) with efficient EMFPA implementation produces errors lower than most methods in literature while maintaining computational efficiency. The performance of reconstruction and advection is visualized in Fig. 3.

5. Curvature Calculation and Surface Tension

Accurate curvature calculation is critical for surface tension force evaluation via the Continuum Surface Force (CSF) formulation, $\mathbf{F}_{ST} = -\sigma\kappa\nabla f$, where σ is the surface tension coefficient and κ is the interface curvature. Several approaches are implemented for curvature estimation. The convolution-based method (K_6 kernel) smooths the volume fraction field prior to derivative evaluation, while Height Function methods compute interface heights along coordinate directions. In addition, PCIC-based approaches derive curvature directly from circular interface representations. The Height Function method of Hernández et al. (2008), employing a variable template (HF-H), adapts to local interface thickness and maintains accuracy even for thin interfaces, demonstrating consistent first-order convergence across both simple and complex geometries.

To further enhance accuracy, two hybrid strategies—H1-PCIC and H2-PCIC—combine PCIC-based interface geometry with Height Function curvature evaluation. In H1-PCIC, the curvature radius is obtained from the Height Function method, while the interface centre is determined using the perpendicular bisector from C^0-corrected PLIC; in H2-PCIC, the curvature radius is similarly obtained from the Height Function method, but the center is determined through curve fitting. These hybrid methods exhibit superior performance in static drop tests, reducing parasitic currents by 2–3 orders of magnitude compared to conventional approaches.

6. Validation Results

THYC-MP was validated against a comprehensive suite of benchmark problems. In the static drop test, the method demonstrated minimal parasitic currents along with accurate prediction of the Laplace pressure jump across the interface. For the dam break problem, the surge front propagation and water level evolution showed good agreement with experimental data reported by Lobovský et al. in literature. In the capillary wave problem, the decay of wave amplitude matched the analytical solution of Prosperetti (1981). Finally, in the simulation of rising bubble problem (Fig. 4), the centre-of-mass trajectory and rise velocity were found to be in close agreement with benchmark solutions presented by Hysing et al. (2009). Two cases of bubble rise representing different ratios of gravitational (buoyancy) to surface tension forces are simulated. The ratio of the two forces is represented by the Eotvos number i.e., $Eo = \Delta\rho g L^2/\sigma$, where $\Delta\rho$ is the density difference between the two fluids, g is the gravitational acceleration. L is the characteristic length, σ is the surface tension. Case 1 corresponds to Eo while case 2 corresponds to $Eo = 125$. The evolution of interface during a bubble rise transient is shown in Fig. 4. Case 2 that corresponds to a relatively weaker surface tension and stronger buoyancy sees faster rise and a pinch off event. The predicted positions of the rising bubble as a function of time for the two cases are compared against benchmark results in Fig. 4.

7. Application to Corium Transport

To investigate the hydrodynamics of corium relocation during severe accident scenarios, the problem of molten corium jet injection into a liquid sodium pool is considered. In the present formulation, the process is modelled as an immiscible two-phase flow without phase change, thereby isolating the

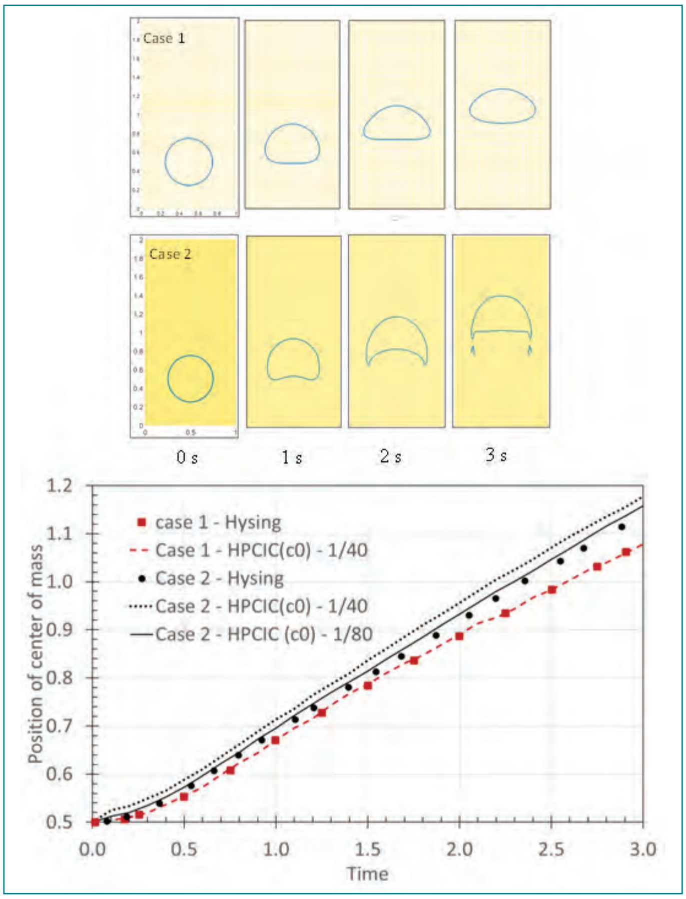

Fig. 4: Rising bubble benchmark—bubble configurations and centre-of-mass position, compared against Hysing et al. (2009) for two test case

interfacial dynamics and breakup behaviour of the jet. The solver was applied to simulate corium jet injection into liquid sodium at inlet velocities of 0.5, 5, and 16 m/s on uniform grids with resolutions of 1 mm and 0.5 mm. The simulations captured key phenomena including jet breakup, interface dynamics, and temperature field evolution. Parallel studies were also performed for Woods metal injection into water. As the current two-phase solver does not incorporate phase change, these simulations were carried out without phase change effects. In parallel, a separate phase change module based on the enthalpy–porosity method has been developed and validated against melting and solidification benchmarks. Results from a representative simulation of corium injection into sodium are presented in Fig. 5, demonstrating the capture of complex flow instabilities and the resulting rich flow structures.

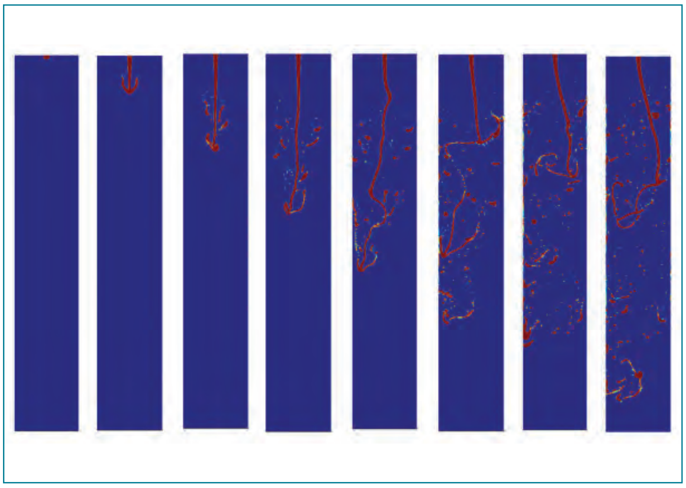

Fig. 5: Simulation results for injection of a 5 mm molten corium jet into liquid sodium at an inlet velocity of 0.5 m/s in a 75 mm × 500 mm cavity. The simulations were performed using THYC-MP on a 150 × 1000 grid

8. Conclusions

This work presents the development of an in-house comprehensive computational framework for simulating two-phase flows with phase change, aimed at severe accident analysis in sodium-cooled fast reactors. Key advances include a novel PCIC method that achieves C^0 continuity allowing high-accuracy interface reconstruction and an analytical formulation of the Edge-Matched Flux Polygon Algorithm (EMFPA) for efficient and accurate interface advection. In addition, hybrid curvature models combining a geometric approach with a variable template height function, along with a force-balanced solver, enable accurate surface tension representation while eliminating spurious currents. The resulting THYC-MP code has been successfully validated against analytical, experimental, and benchmark problems, and is capable of handling large density ratios, complex interface dynamics such as breakup and coalescence, and strong surface tension effects. Ongoing developments focus on extending the solver to incorporate phase change physics, enabling three-dimensional and parallel simulations, and expanding validation against experimental databases. These capabilities are expected to support severe-accident analysis in sodium-cooled fast reactors, including fuel–coolant interaction and post-accident heat-removal scenarios.

Shri SOURABH AGARWAL
Materials Chemistry & Metal Fuel Cycle Group
Indira Gandhi Centre for Atomic Research
Kalpakkam, Tamil Nadu, India

LECTURE SERIES

Pyrochemical Reprocessing: Principles, Process and Perspectives

Rapid growth of Indian Fast Breeder Reactor (FBR) program is needed to move quickly towards use of our vast thorium reserve. These needs, use of metal fuels in FBRs because of its high breeding ratio and lower doubling time. Also to lower the overall doubling time metallic fuel reprocessing using pyroprocessing is most suitable because it can easily manage short cooled high burnup fuel. Pyroprocessing or pyrochemical reprocessing is a non-aqueous high temperature reprocessing method and molten salt electrorefining based pyroprocessing is most suitable for metal fuels. The separation of actinides from fission products is based on the thermodynamic stabilities of their chlorides and the equipment where this separation is carried out is called as Electrorefiner (Fig. 1). An Electrorefiner consists of an anode and a cathode dipped inside a molten salt (eutectic mixture 44 wt.% of LiCl 56 wt.% of KCl) having 2–5 wt.% UCl_3. Spent fuel will be loaded into the anode basket and solid cathode will be inserted first. As chlorides of Alkali Metals (AM), Alkali Earth Metal (AEM) and Rare Earth (RE) Fission Products (FP) are most stable, they easily come out from the anode and dissolve in the electrolyte by replacing UCl_3 whereas chlorides of Noble Metals (NM)FP and clad material are least stable and so these metals remain in the anode basket. The stabilities of Actinides chlorides are in between and so they dissolve at anode and deposit at cathode when potential is applied. Initially only Uranium will deposit in solid cathode and once the plutonium to uranium concentration ratio in the electrolyte raises U & Pu along with Minor Actinides Co-deposits in liquid Cadmium cathode. So, in summary actinides get separated from noble metal FPs at anode and from AM, AEM & RE FPs at cathode. The whole flowsheet for pyroprocessing based on molten salt electrorefining can be divided into three main

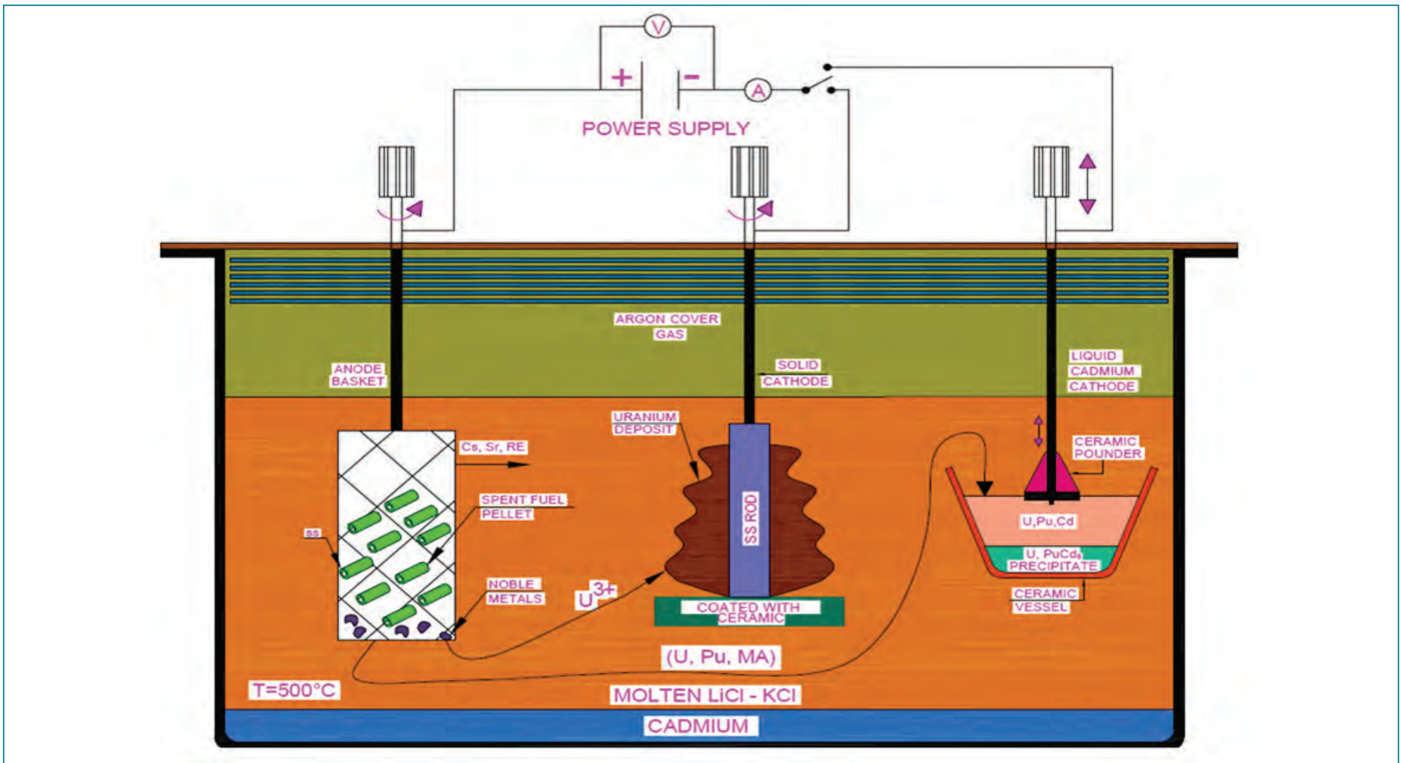

Fig. 1: Molten salt electrorefiner schematic

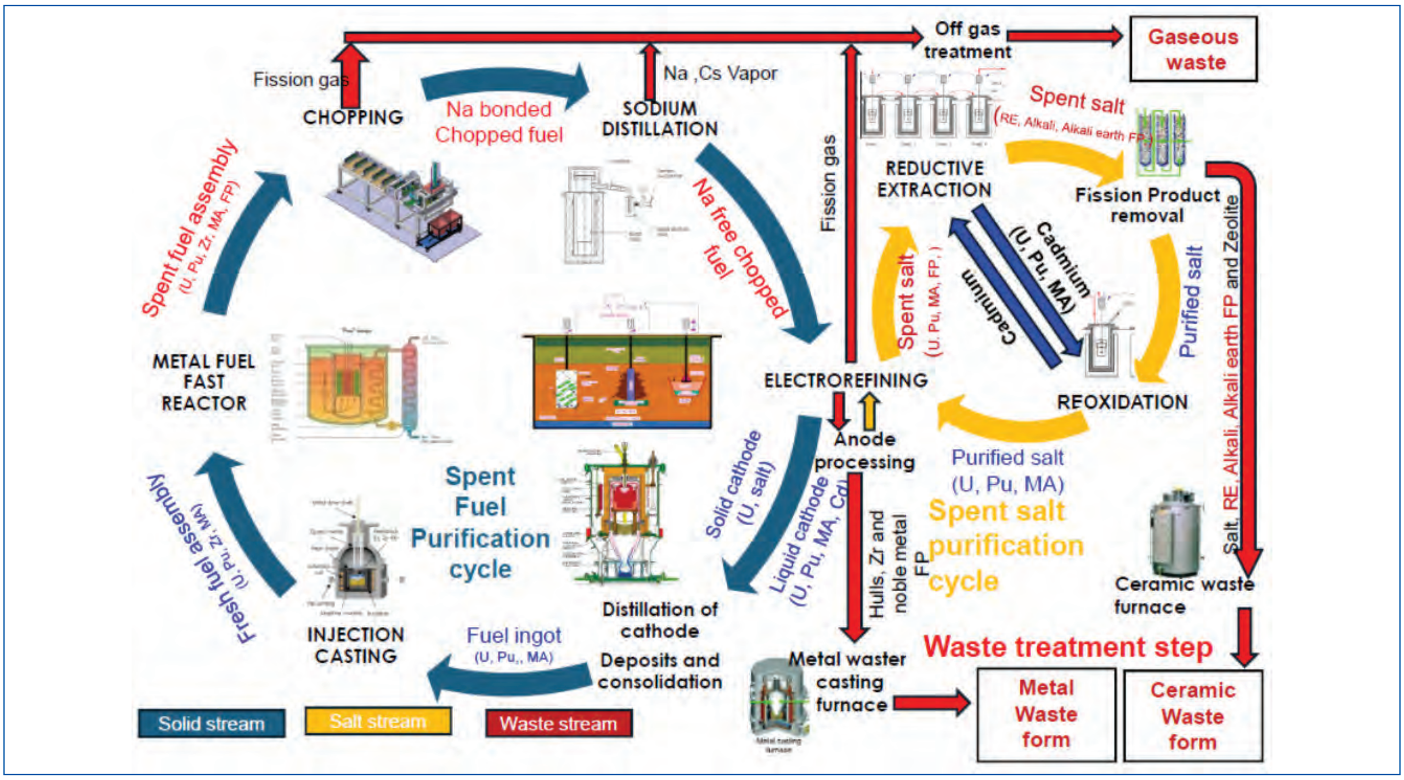

Fig. 2: Pyrochemical reprocessing process flowsheet

streams i.e. spent fuel purification cycle, spent salt purification cycle and waste streams (Fig. 2).

IGCAR has been developing pyroprocessing techniques. Initially, efforts focused on handling LiCl-KCl eutectic, designing equipment, and preparing uranium alloys, gaining skills in glove box purity and induction melting. Later, facilities for processing uranium in small batches were established, leading to research on other process steps and plutonium-based alloys. The PyroProcess R&D Facility (PPRDF) was developed to demonstrate electrorefining and cathode processing of U-Zr alloy in larger batches with remote handling. In PPRDF, significant progress was made, such as maintaining high purity argon environment inside 500 m^3 Containment box at negative pressure, preparation of 1 ton of purified molten salt and transferring it inside Electrorefiner in hot condition by pressure transfer. Successful demonstration of engineering scale Electrorefining experiments with U metal, chopped sodium bonded U-Zr fuel pin with Clad and later vacuum distillation and melting of uranium dendrites (Fig. 3) were also carried out.

Future developments aim to demonstrate other important process steps in engineering scale like spent salt purification and immobilizing fission products. A used salt treatment facility (USTF) (Fig. 4) will demonstrate spent salt purification in engineering scale. Efforts on waste treatment are ongoing, with laboratory-scale activities and engineering-scale demonstrations planned. To get experience of pyrochemical reprocessing with actual metallic spent fuel a hot-cell facility called as Metal Fuel Cycle Demonstration Facility (MFCDF) is planned in adjacent to proposed FBTR 2. Eventually, a full-scale pyroprocessing plant will be developed, followed by facilities for commercial metal fuel fast reactors.

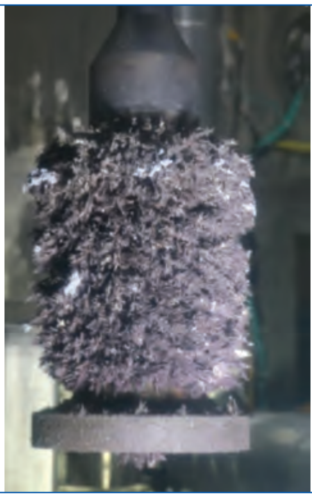

Fig. 3: Uranium dendrite deposited over solid cathode

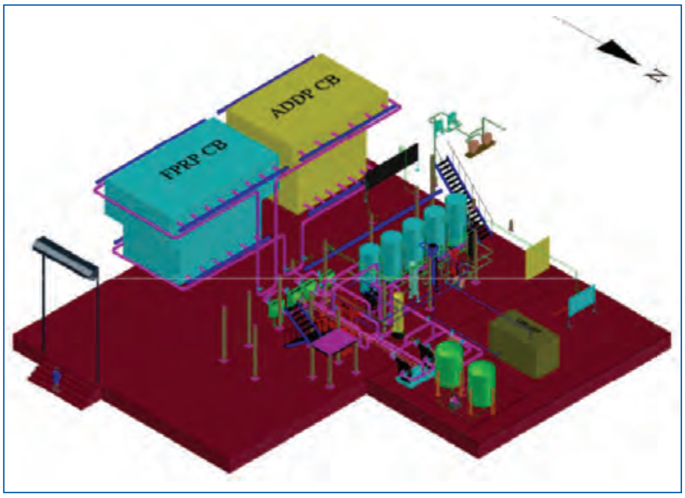

Fig. 4: 3D view of USTF facility

Dr. M. BOOTHARAJAN
Materials Chemistry & Metal Fuel Cycle Group
Indira Gandhi Centre for Atomic Research
Kalpakkam, Tamil Nadu, India

LECTURE SERIES

Non-destructive Assay of Actinides using In-house Established Hybrid-KED/ Calorimetry Techniques

Hybrid-K-Edge/K-XRF Densitometry

A non-destructive and noninvasive technique is preferable for characterization of the spent fuel solutions in the reprocessing plants, especially samples associated with high radiation dose. A hybrid K-edge/KXRF densitometer (HKED) technique has been designed, fabricated, and commissioned indigenously (Fig. 1) to accomplish the above objective for the spent fuel solutions from Compact reprocessing facility for advanced fuels in lead cells (CORAL), Kalpakkam.

Initially, the mass attenuation coefficient of uranium was determined using a uranium standard solution with concentration established by both potentiometric and gravimetric methods. The HKED system was calibrated with a uranium standard solution whose concentration was determined potentiometric method. The results obtained from the K-edge and potentiometric methods were compared and showed an agreement within ±3%. Similarly, the mass attenuation coefficient of thorium was determined using a pure thorium solution. Further, mixtures of actinides, namely U–Th and U–Pu solutions over different concentration ranges, were prepared. The results for uranium obtained by nondestructive (HKED) and destructive (mass spectrometry and potentiometric) methods were compared, and the percentage error between these methods was found to be within ±5%. Validation of the HKED results with conventional methods, such as potentiometry, confirms that this technique is suitable for estimating uranium and plutonium in solutions from the reprocessing plant (CORAL). Additionally, a high-dose dissolver solution from CORAL was analyzed, and the concentrations of uranium and plutonium were determined and compared with thermal ionization mass spectrometry results, showing an error within ±5%. This technique does not require dilution, addition of reagents, or separation of elements. As a non-destructive method, K-edge densitometry generates negligible secondary waste and minimizes radiation exposure to personnel. Therefore, this technique has strong potential to replace conventional destructive and separation-based methods currently used for determining concentrations of special nuclear materials in reprocessing plants.

Fig. 1: Hybrid K-edge /K-XRF facility

Calorimetry Techniques

Conventionally, quantitative estimation of radionuclides is carried out by measuring the decay particles/radiation (alpha, beta, neutron/gamma) or electrochemical techniques (potentiometry). Calorimetry is an alternative non-destructive technique for quantitative estimation of radionuclides, especially plutonium-containing fuels. The measurement of total heat in terms of power associated with radioactive decay is the basis of this calorimetry technique. This technique is widely used in the nuclear industry to account for plutonium in fuel pellets, powders, and metals. Fig. 2 shows the in-house developed twin cell calorimeter. For this, a calorimeter was designed and developed in-house and its application in preliminary studies for estimation of plutonium in mixed uranium plutonium oxide fuel (PFBR). Initially, the calorimeter was calibrated electrically using joule heater and sensitivity

Fig. 2: Twin cell calorimeter

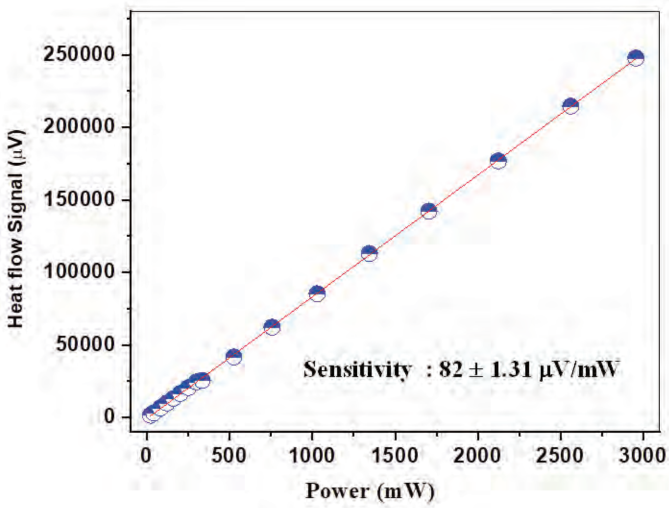

Fig. 3: Electrical calibration for 20–3000 mW

was found to be 82 ± 1.31 µV/mW. The sensitivity of the calorimeter was validated using MOX pellets and tritium standards. Fig. 3 shows the electrical calibration of calorimeter using joule heater for the power range from 20 to 3000 mW.

The assays were carried out for a longer duration (~24 h) till the signal reaches a near constant value. Baseline fluctuation of the signal was found to be a key parameter to minimize the error. Thus, baseline measurement was carried out before and after each sample measurement. An average baseline value with relative standard deviation was less than 3% was used to determine the net signal for all the samples. The plutonium in unknown MOX samples and U–Pu–Zr metallic fuel samples were estimated and the results were corroborated with the data from potentiometric methods and shown below in Table 1. The error in the estimation of plutonium (~1 g) is found to be ±5%.

Table 1: Comparison of results of plutonium weight obtained by potentiometry and calorimetry

MOX Group ID	Weight of Pu by potentiometry (g)	Calorimetry				Error (%)
		Average net signal (µV)	RSD (%)	Total power* (Ps) (mW)	$M_T = P_S/P_{eff}^{\#}$ Wt of Pu (g)	
A	0.3218	144 ± 8	2.68	1.585	0.2700	−16.09
B	0.6311	399 ± 4	0.69	4.391	0.7482	18.55
C	0.9936	509 ± 10	0.90	5.601	0.9544	−3.94
D	1.2792	723 ± 6	0.80	7.956	1.3557	5.98
E	1.6341	896 ± 8	0.44	9.860	1.6801	2.81
F	1.9514	996 ± 5	0.43	10.961	1.8676	−4.29
G	2.2822	1280 ± 10	0.67	14.086	2.4001	5.16
H	3.2745	1759 ± 15	0.81	18.807	3.2045	−2.14
I	4.2718	2235 ± 23	0.78	24.596	4.1909	−2.51
J	4.9309	2642 ± 26	0.80	29.075	4.9540	0.47

Dr. S. AMIRTHAPANDIAN
Materials Science Group
Indira Gandhi Centre for Atomic Research
Kalpakkam, Tamil Nadu, India

LECTURE SERIES

Role of Electron Microscopy to Study Irradiation Effects in Materials

Transmission Electron Microscopy (TEM) and Scanning Electron Microscopy (SEM) differ primarily in that TEM transmits electrons through ultra-thin samples to image internal structure via 2-dimensional images, while SEM bounces electrons off surfaces to create detailed 3-dimensional topographic images. Both the electron microscopy techniques play an important role in understanding the ion irradiation effects in materials.

Mainly, transmission electron microscope (model: LIBRA 200FE, make: Carl Zeiss) operating at 200 kV equipped with in-column energy filter was extensively used for these works. The information limit of the microscope is 0.13 nm. TEM specimens of the samples (thoria, zirconia, IPG, yttrium titanates) were prepared by scratching the surface of the pellets using a scalpel blade and by dispersing it in the carbon coated copper grid with the help of propanol.

Alloy D9 is a void-swelling resistant nuclear grade austenitic stainless steel (SS) based on AISI type 316-SS in which titanium constitutes an added predetermined alloying composition. Systematic analysis on the void swelling behaviour of D9 alloys were carried out in our lab. The identification of the peak swelling temperature involves determination of swelling through a range of irradiation temperatures. The methods for obtaining estimates of swelling in ion irradiation experiments are (i) by direct observation of voids at the peak damage region using TEM and (ii) by measurements of the gross swelling by surface profilometry. In our earlier work, by comparing the peak swelling temperature determined by conventional step height measurement and Positron Annihilation Spectroscopy (PAS) measurement, it was found that the peak swelling temperature using PAS was 50 K higher and we have conjectured that the positrons trapping in the irradiation induced TiC precipitates and it could have caused the shift in peak swelling temperature. However, to confirm this conjecture, TEM studies were extensively carried out and irradiation induced TiC precipitates were clearly observed in TEM images with Moiré fringes (Fig. 1) where dislocation-controlled TiC precipitates are clearly seen. The lattice spacing of austenite matrix and TiC precipitates are nearly identical

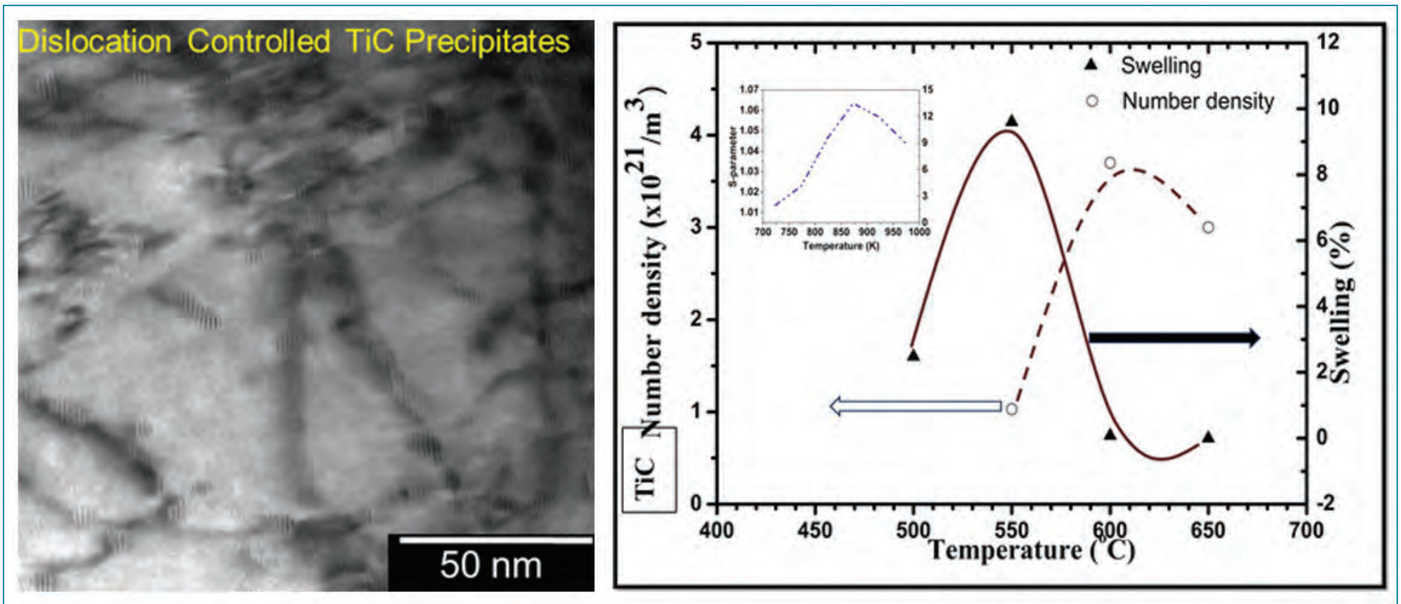

Fig. 1: TEM image of dislocation-controlled TiC precipitates in D9 alloy & void swelling and TiC number density as a function of irradiation temperature

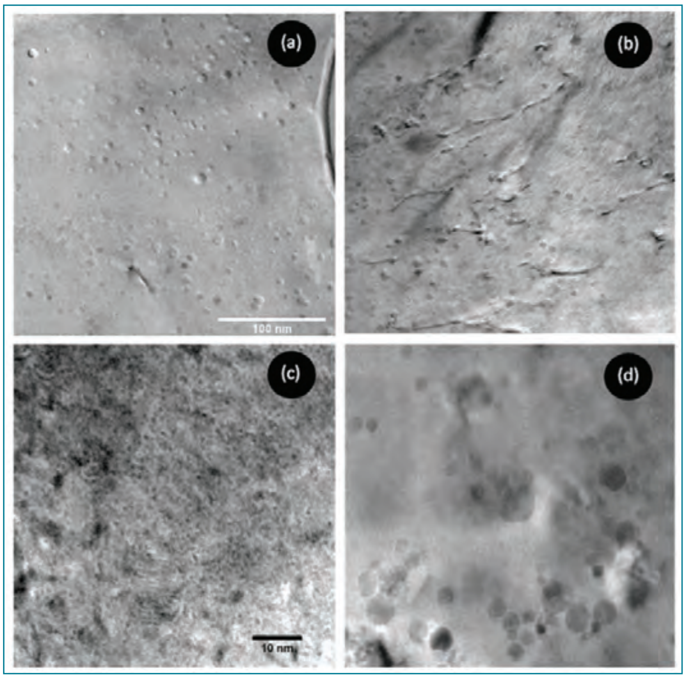

Fig. 2: Low magnification bright field TEM images of the Fe14Cr-0.2Ti-0.3Y_2O_3 alloy (a) as-prepared; (b) 5 MeV Ni^{2+} ion irradiated alloy samples for the dose of 40 dpa at 600 °C; (c) 40 dpa at 700 °C; and (d) annealed at 700 °C for 6 h (scale bar shown in (a) applies for (b) and (d) also)

and hence there is a formation of Moiré fringes wherever TiC precipitates are present.

In the case of oxide dispersion strengthened steels, two different ODS alloys of composition Fe-0.2Ti-0.3Y_2O_3 and Fe-14Cr-0.2Ti-0.3Y_2O_3 with 5 MeV Ni^{2+} ion beam to 150 dpa at 700 °C and 600 °C at JANNUS irradiation facility and by examining the effects using transmission electron microscope. The TEM results of Fe14Cr-0.2Ti-0.3Y_2O_3 alloy (Fig. 2) clearly show the drastic reduction in particle size along with increase in particle density and it is more pronounced in the sample irradiated at 700 °C (i.e, the particle density changes from $5.2 \times 10^{20}/m^3$ (as-prepared) to $8 \times 10^{23}/m^3$ (irradiated)). This can occur only when nucleation of oxide particles in Fe matrix along with inverse Oswald ripening.

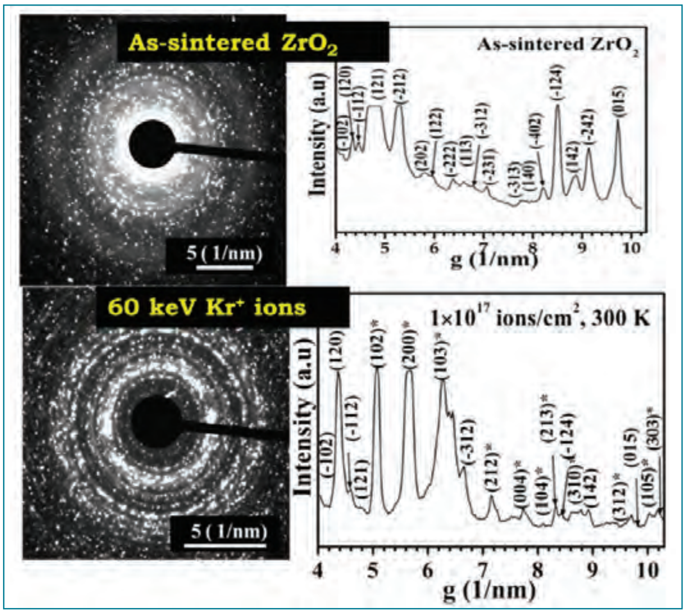

Fig. 3: Electron diffraction pattern of as-sintered and 60 keV Kr^+ ion irradiated ZrO_2 sample, monoclinic to tetragonal phase transformation is observed

The stability of the oxide dispersoid (Y_2TiO_5 and $Y_2Ti_2O_7$) eventually depends on the strength and the nature of the metal–oxygen (M–O) bonds. Electron energy loss spectroscopy (EELS) analysis showed that Ti-O bonds in $Y_2Ti_2O_7$ is more covalent compared to Y_2TiO_5. Further DFT results showed that the M-O bonds in $Y_2Ti_2O_7$ are found to be more covalent than in Y_2TiO_5. Hence it is suggested that $Y_2Ti_2O_7$ is better radiation resistant than Y_2TiO_5.

In the case of ZrO_2, detailed TEM investigations (Fig. 3) were carried out to understand the ion irradiation induced monoclinic to tetragonal phase transformation which is local stress driven phase transformation. The amount of the transformed phase (tetragonal) was found to be higher in the case of ion irradiation at 143 K. TEM investigations show bubble induced swelling. The bubble induced swelling was

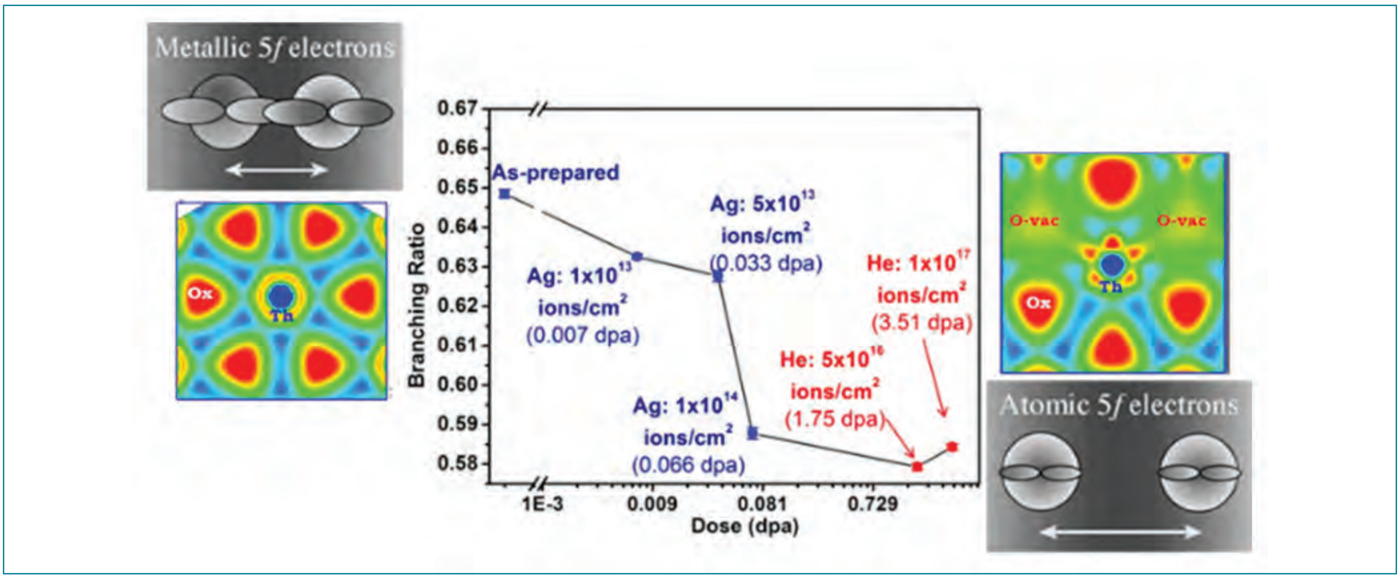

Fig. 4: The Branching ratio of Th N_{45} edges calculated from the EEL spectra. The Branching ratio reduces with increase in damage (dpa) showing a transition from metallic to atomic nature in Th atom

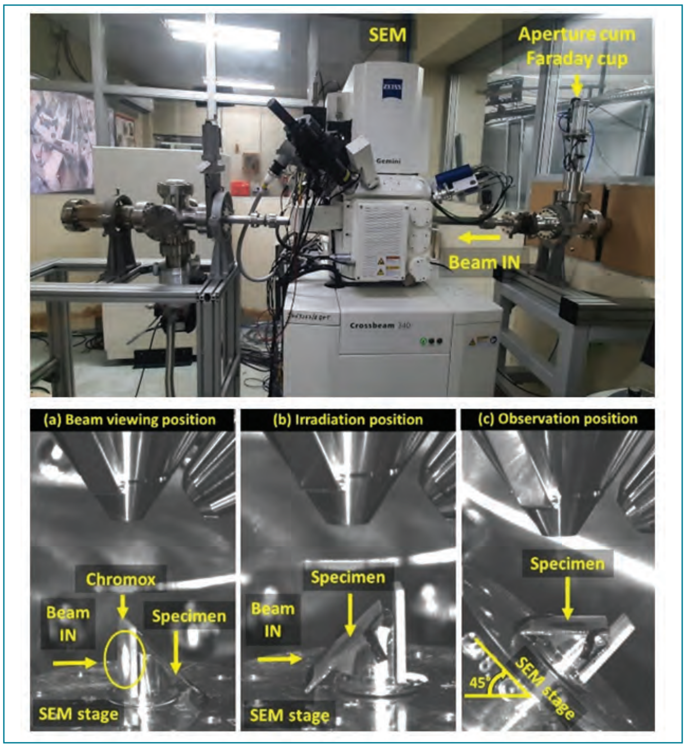

Fig. 5: Photograph of i^4 FESEM facility and different positions of SEM stage

found to be low when the ion irradiation was carried out at 143 K and it is attributed to the immobility of the defects at such low temperatures. The oxygen vacancy concentration dictates the phase transformation (induced by stress) and swelling (relive the stress by bubble formation).

In the case of ThO_2, the behaviour of the inert gas helium, in the thoria, was studied by implanting helium using low energy beam (100 keV He^+). GIXRD and TEM experiments showed that there is lattice expansion (1.07%) in isolated nanometric regions in the surface of the sample upon irradiation. First principle calculations showed that the energetics prefer aggregation and ordering of helium in the octahedral interstitial sites in thoria lattice, and the ordered aggregation of helium results in lattice expansion of 1.25%. The expansion calculated from DFT is in agreement with experiments. Further, Th N_{45} edges in the EELS spectra of the as-prepared and ion irradiated thoria samples. The branching ratios were calculated from the N_{45} edges and the expectation values of the 5*f* spin-orbit interaction per core hole $\langle w^{100} \rangle / n_h$, were calculated using the branching ratio. The branching ratio B is defined as $B = A_{5/2} / (A_{5/2} + A_{3/2})$, where $A_{5/2}$ and $A_{3/2}$ are the integrated intensities of N_4 and N_5 peaks respectively. In the present results (Fig. 4), when the damage increases, the branching ratio decreases from 0.649 to ~0.58, this shows that n tends to decrease upon ion irradiation, indicating that the occupancy of 5*f* orbital in thorium tends to become atomic in nature, upon ion irradiation. Charge density difference, calculated from DFT calculations, showed that in the case of perfect thoria, the 5*f* electrons are largely hybridized. But when O-vacancies were present, the electron distribution is drastically modified. The electron density around the Th atom clearly manifests the shape of 5*f* orbital of atomic Th. Thus, the irradiation damage causes a transition from metallic-like to atomic-like nature in the *f* orbitals. One of the consequences of this transition could be a rise in the unit cell volume.

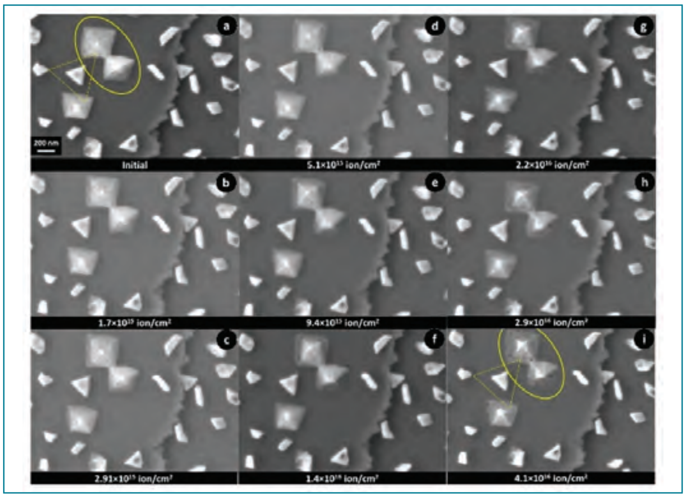

Fig. 6: Sequence of SEM images showing the evolution of Sb islands on sapphire substrate under 2 MeV Al^+ ion irradiation. The images were recorded (a) before irradiation, and after irradiation at the following ion fluences (b) 0.17, (c) 0.29, (d) 0.51, (e) 0.94, (f) 1.4, (g) 2.2, (h) 2.9 and (i) 4.1 $\times 10^{16}$ ions/cm^2

We have recently established a new facility named *in-situ* ion irradiation and imaging with Field Emission Scanning Electron Microscope (i^4-FESEM) facility (Fig. 5) at Indira Gandhi Centre for Atomic Research (IGCAR), Kalpakkam. This *in-situ* ion irradiation and imaging facility is the first of its kind in India and third of its kind in the world. Thin film of antimony was deposited on a sapphire (c-Al_2O_3) substrate via Molecular Beam Epitaxy (MBE). The base pressure in MBE chamber was $\sim 2 \times 10^{-10}$ mbar, and the substrate temperature was held at 245 °C, yielding a 500 Å antimony layer. SEM characterization of the deposited layer showed the formation of nanometer-sized antimony islands exhibiting diverse morphologies, such as square pyramids and triangular islands. This specimen was used for *in-situ* experiment. Fig. 6 shows the sequence of SEM micrographs of antimony islands evolving with ion fluence. It was observed that there is reduction in diagonal length in the case of islands with square pyramid morphology. The square pyramids seem to have decomposed or dissociated while islands with triangular morphologies remained stable. During 2 MeV Al^+ ion irradiation, the electronic energy loss (S_e) is 1.7 keV/nm, which is not high enough to form ion tracks in sapphire. However non-melting thermal spikes are expected to form. A "non-melting thermal spike" refers to a localized, intense burst of heat within the material that, along the ion path. It causes a significant temperature increase, but doesn't cause the surrounding material to melt. This rise in lattice temperature is sufficient to induce evaporation, and diffusion processes and modify the Sb surfaces.

Dr. PRASHANT SHARMA
Fast Reactor Technology Group
Indira Gandhi Centre for Atomic Research
Kalpakkam, Tamil Nadu, India

LECTURE SERIES

Design and Development of Sensors for Sodium Systems

Sodium instrumentation consists of mainly measurement of sodium level, leak, temperature and flow rate. Sodium is a unique coolant which has some physical properties like density and viscosity similar to those of water whereas thermal conductivity and electrical conductivity are significantly different from those of water. At the same time, sodium reacts with water and oxygen and these reactions can not only lead to fire but also generate some corrosive products like NaOH. Therefore for sodium instrumentation preference is usually given to those instruments where penetrations in sodium systems are minimal and where chances of sodium coming in contact with air/water are also minimal. Due to superior electrical conductivity of sodium, many of the sensors are electrical conductivity based sensors.

The sensors for sodium level measurement utilize electrical conductivity of sodium and their design has significantly evolved with time and operating experience. The initially developed sensors were contact based sensors where a physical contact of the sensing element with liquid sodium used to give an indication. In this category mainly two types of sensors were there namely – Spark Plug Based Level Probe (SPLP) and Resistance Type Level Probe (RTLP). The SPLP consists of an extended nickel wire attached to the base of a modified spark plug. As liquid sodium in a tank or vessel touches the tip of the nickel wire an electrical signal is generated. The sensor was simple in construction yet many a times due to deposition of sodium aerosols spurious signals were generated. This led to development of another contact based sensor – Resistance Type Level Probe (RTLP) which operated on principle of change in overall electrical circuit resistance when sodium contacted the stainless steel pocket of the probe inside which a copper rod was brazed. The output of the probe was not affected by sodium aerosols but its output was dependent on sufficient wetting in liquid sodium. Moreover, fixing this probe required welding in sodium vessel or tank which implied that in case of maintenance, these joints need to be cut and re-welded.

To overcome these limitations, mutual inductance based discrete and continuous level probes were developed. These probes were non-contact based and work on the principle that the mutual inductance of secondary winding w.r.t. primary winding (and therefore the secondary voltage also) reduces due to electrical eddy currents in sodium surrounding the probe. Here, the primary and the secondary windings are housed inside an austenitic stainless steel pocket and do not

RTLP

MI Discrete LP

MI Continuous LP

Sodium Aerosol Detector

come in contact with sodium which significantly eases the maintenance, if any, for these probes. Since the electrical conductivity of sodium reduces with temperature and therefore the corresponding eddy currents also, an external resistance based temperature compensation method was utilized for achieving temperature compensated output.

For detection of sodium leak in spaces where it is possible to collect leaked sodium such as bellow sealed valves and leak collection trays, spark plug based leak detectors are used. They work on the same principle as spark plug based level probes. Extended Spark Plug type Leak Detector (ESPLD) is another type of contact based leak detector which is used when the sensor has to be inserted in highly narrow and curved paths. For leak detection on pipelines and components covered with thermal insulation, wire type leak detectors are used. These detectors consist of a nickel wire with ceramic beads. When sodium comes in contact with these wires, the sodium electrically grounds the nickel wire and an alarm is generated electronically. A lot of R&D has been carried out to determine the optimum layout of these detectors not only for horizontal and vertical pipelines but also for various shapes of vessels. Mutual Inductance based Leak Detectors (MILDs) are miniaturized non-contact type leak detectors which are used in those places where it is not possible to insert other sensors.

For global leak detection in a facility or area, a sodium aerosol based detection system is utilized. This system consists of sampling fluted pipes routed in the entire facility and connected to a blower. At the outlet of the blower, the outgoing gas is sampled and sent to a Sodium Aerosol Detector (SAD). When the gas passes over the heated platinum filament of the SAD, preferential surface ionization of sodium present in sodium bearing compounds takes place and positive sodium ions are liberated. These positive ions then migrate to the cathode which is kept at a negative potential. This motion of charged particle generates electrical current which is detected by extremely sensitive electronic circuit. An alarm gets generated if value of this current is significantly higher than the background value. This SAD based system is very sensitive and can detect even very small leaks in the sampled area.

Measurement of sodium temperature is carried out by K-type thermocouples which work on the phenomenon of Seebeck effect. Cold junction temperature compensation is done electronically for these thermocouples. The thermocouples along with data acquisition and control system play a very important role in maintaining proper temperature in various systems and facilities.

Fire detection in sodium systems is carried out by diverse and redundant systems consisting of smoke detectors, sodium aerosol detectors. Recently, a visual image analysis system based on artificial intelligence has also been developed and deployed for sodium fire detection.

For sodium flow measurement also, conventional flow meters used for water such as venturimeter, rota-meters are not employed rather electrical conductivity based electromagnetic flow meters are used. There are two types of flow meters in this category – Permanent Magnet Flow Meter (PMFM) and Eddy Current Flow Meter (ECFM). The PMFM works on the principle that when an electrical conductor, such as sodium, moves under the influence of a perpendicular magnetic field, an EMF (proportional to the velocity) is produced across the conductor. The ECFM works on the principle of distortion of magnetic field due to eddy currents in flowing sodium. This distortion in magnetic field gives rise to a voltage difference between the two coils. This voltage difference is proportional to velocity of liquid metal.

All these sensors were developed and their performance was evaluated in sodium loops of IGCAR. Based on their satisfactory performance these sensors were recommended for PFBR. The operating experience of these sensors in actual reactor environment has been quite satisfactory and has validated their design.

Shri G. RAMESH
Safety, Quality & Resource Management Group
Indira Gandhi Centre for Atomic Research
Kalpakkam, Tamil Nadu, India

Lecture Series

Quality Assurance Challenges during Mechanical Construction of FBR Projects

Introduction

Quality assurance methodologies provide confidences in complying the stringent technical requirements of components/systems during raw material procurement, manufacture, examination, testing & commissioning activities. Fulfilling stringent technical requirements of these nuclear components/systems necessities demonstration, testing and standardization without compromising both national and international safety regulations. Quality management system based process approach will be the most suitable for the development of new designed components and structures of projects. Promoting indigenization of Fast breeder projects such as prototype fast breeder reactor, demonstration fast reactor fuel reprocessing plant, etc. poses several challenges during design, fabrication, assembly, testing, erection and commissioning including availability of resources. Overall execution and successful performance requires feedback from scaled down test facilities/full-scale components depend on first of its kind (FoK) nature. Quality assurance approaches towards meeting these requirements mandate understanding, technical knowledge, skill and practical experiences. In addition to specific requirements, industry acceptable codes & standards help to improve effectiveness of QA practices. At all the stages of component/system development as given in Fig. 1, quality practices along with national/international standards ensure design intents with safe & reliable performance.

These standards provide a comprehensive frame work to ensure nuclear quality, safety, reliability and compliances. The important eighteen element criteria including the key elements such as safety, quality grading and independent inspection from management function, process implementation, measurement, assessment and improvements were envisaged so as to ensure objectivity, transparency and regulatory confidences. In addition to design/safety classifications, inspect-ability/verification feasibility also considered in nuclear graded approaches.

Reactor Projects: Construction Phase Challenges

Quality assurance approaches (Fig. 2) provides a control over each stage of component/system development processes. The technical requirements from RCC-MR and ASME derive quality specifications for FBTR, PFBR.

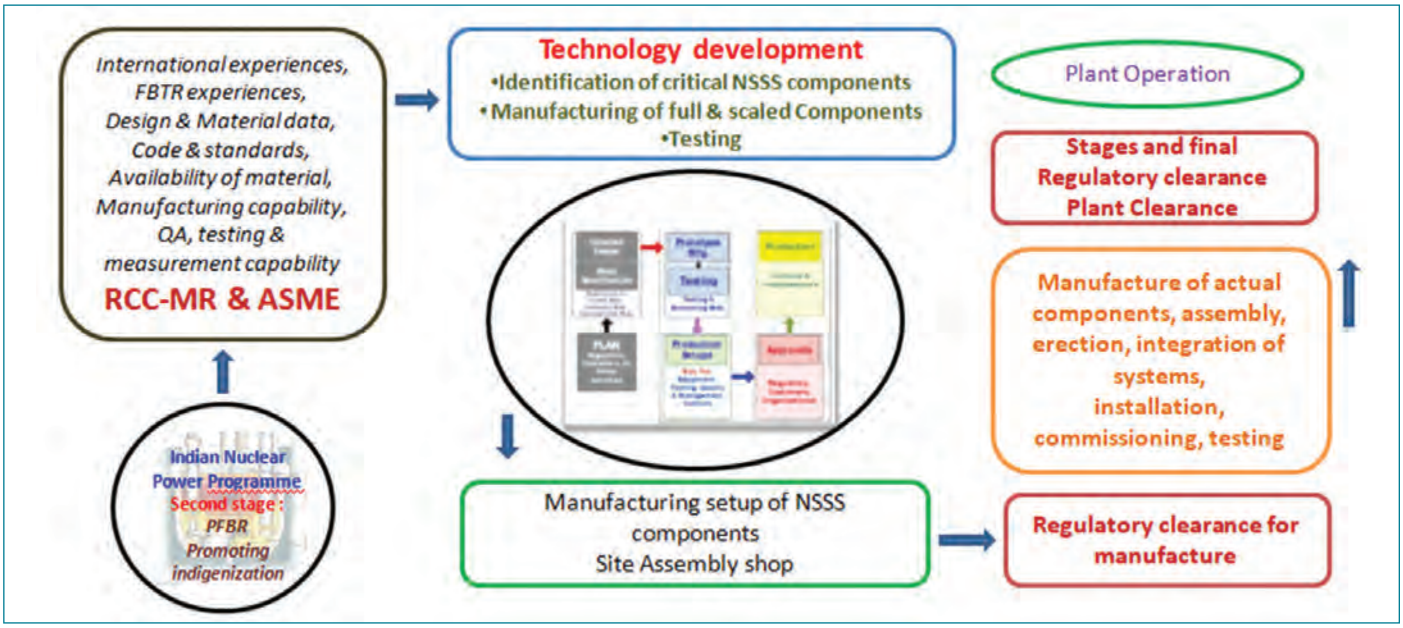

Fig. 1: Process approach for new developments

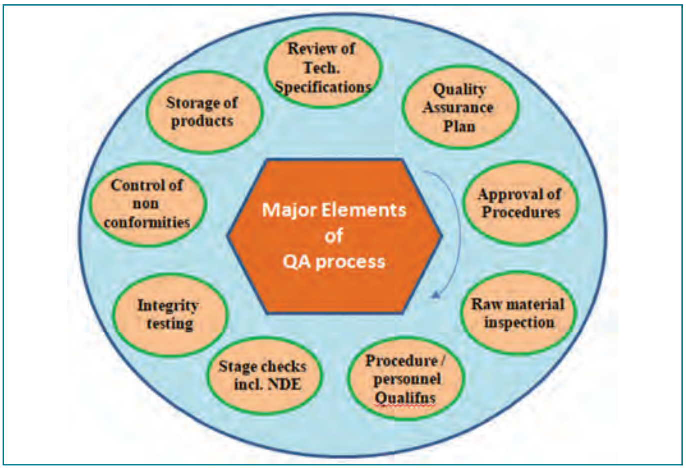

Fig. 2: QA Process for FBR projects

Additional Specifications includes controlled chemical (SS 316LN), mechanical and metallurgical properties such as high temperature tensile, ductility, toughness, delta ferrite, inclusion content, essential welding variables, production test coupons, component assembly in nuclear clean room and nondestructive volumetric examinations with stringent acceptance criteria. Available industrial resources, capabilities, skill & experiences, Challenges in SS 316 material & component qualifications such as reactor vessel pullout, defect free welds, stringent dimensional control with geometric features on large size/slender components, testing methods for meeting higher sensitivities under site conditions were addressed.

Rigorous Quality practices such as profile measurements of main vessel sector, methodologies for establishing axis w.r.t reactor vessel axis using precise optical instruments and to ensure soundness of K-type corner welds (Fig. 3a) using ultrasonic examination procedures during fabrication of FoK components/dynamic mechanisms of PFBR were employed and demonstrated at leading indian industries thus equipping them for easy manufacture of actual reactor components.

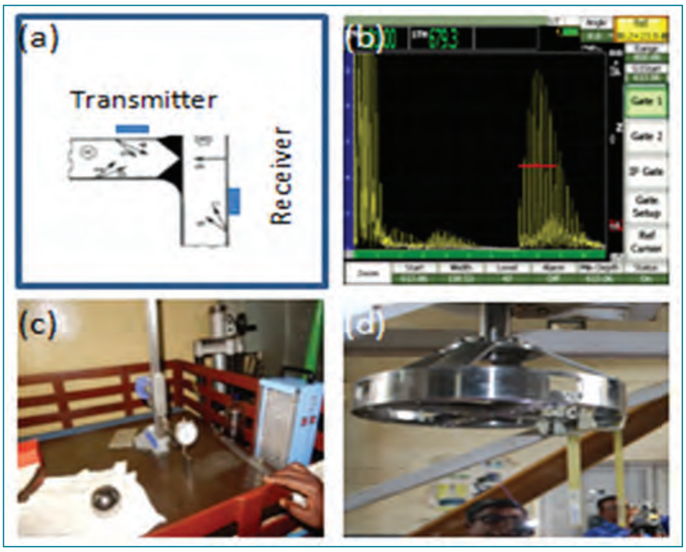

Fig. 3: (a) UE of K-type corner welds of Roof slab sector, (b) presence of solidified sodium in bottom dished end of IHX, (c) dimension inspection of LRP bearing ball, (d) measurement of scanning plane variation using optical instruments

Reactor Projects: Commissioning Phase Challenges

While verifying the performance of components and interconnected piping systems, expected operating characteristics are to be achieved. A deviation in any functional parameter affecting the quality, integrity & safety calls for through review, analysis and if need, refurbishment of components so as to provide the intended performance. During refurbishment, assessed existing condition of the components such as presence of solidified sodium in bottom dished head of IHX (Fig. 3b) and suitable QA plans are designed to mitigate the deviations without compromising parent specifications. To fulfill these quality specifications, several challenges such as dimensional, surface hardness and geometric features during fabrication, inspection and testing were envisaged. Time bound mitigation of these challenges during (i) modification of Annular Linear Induction Pump (ALIP) to control/minimize vibrations; (ii) Load & Spacer Bearing balls (Fig. 3c) of Large & Small Rotable Plugs to enhance superior material properties; (iii) Hard chrome plating for surface hardness 80 microns of coating thickness on outer tube (3.5 m long) of Transfer Arm; (iv) Dummy fuel subassemblies to ensure surface imperfections by through visual examinations and controlling dimensional features for smooth testing of actual fuel subassembly; (v) Plugging of tubes for leak tightness integrity of IHX; (vi) optical measurement of scanning plane variations (Fig. 3d) during rotation of transducer of Under sodium Ultrasonic scanner of PFBR are noteworthy.

Reprocessing Projects: Construction Phase Challenges

Component design and technical requirements from USNRC & ASME codes derive quality specifications based on the severity of service conditions of DFRP & FRFCF. Additional Specifications includes controlled chemical (i.e. Nitric Acid grade, SS 304L), mechanical and metallurgical properties such as Susceptibility to intergranular corrosion resistance under conc. nitric acid service, ductility, toughness, tighter inclusion content, essential welding variables such as heat input, inter-pass temperature control, welder qualifications especially small bore pipe sizes under site simulated difficult positions and nondestructive volumetric examinations with stringent acceptance criteria. Available industrial resources, capabilities, skill & experiences, Challenges in SS 304L and titanium grade 2 material & component qualifications such as dissolver, annular tanks, waste storage tanks, etc., defect free welds in dense piping systems, testing methods for meeting higher sensitivities with audit on radiographed welds were addressed.

Summary

Quality assurance approaches for the nuclear installations have been well established and documented to provide sufficient confidences on the FoK components & systems within the regulatory frame works.

Dr. N. RAMANATHAN
Materials Chemistry & Metal Fuel Cycle Group
Indira Gandhi Centre for Atomic Research
Kalpakkam, Tamil Nadu, India

LECTURE SERIES

CHEMISTRY OF COLD-ISOLATED MOLECULES

Chemistry of cold-isolated molecules explores molecular behavior under conditions where thermal motion is drastically reduced and intermolecular interactions are minimized. By trapping molecules in inert cryogenic matrices, it becomes possible to observe intrinsic molecular properties with exceptional clarity. Such conditions provide a unique opportunity to investigate molecular structure, conformational preferences, reaction pathways, transient species, and weak intermolecular interactions that are often obscured under ambient conditions. Cold isolation provides a unique molecular microscope, revealing the fundamental principles governing molecular structure, dynamics, interactions, and reactivity with unprecedented clarity.

Molecules are not static objects; they are dynamic entities continuously exploring different spatial arrangements through rotations about chemical bonds. These subtle structural variations, known as conformations, profoundly influence molecular stability, reactivity, interactions, and function. Under ordinary conditions, however, thermal motion and intermolecular interactions often obscure delicate molecular details. To truly understand molecular behavior, it becomes essential to study molecules under simplified and controlled environments where intrinsic molecular properties can emerge with clarity.

Conformations are isomers interconvertible through rotation about single bonds without altering the molecular framework. The influence of conformations extends across biology, chemistry and materials science. The conformational organization of DNA enables stable information storage and replication, while enzyme activity depends on dynamic conformational adjustments that create highly specific catalytic environments. In medicinal chemistry, subtle

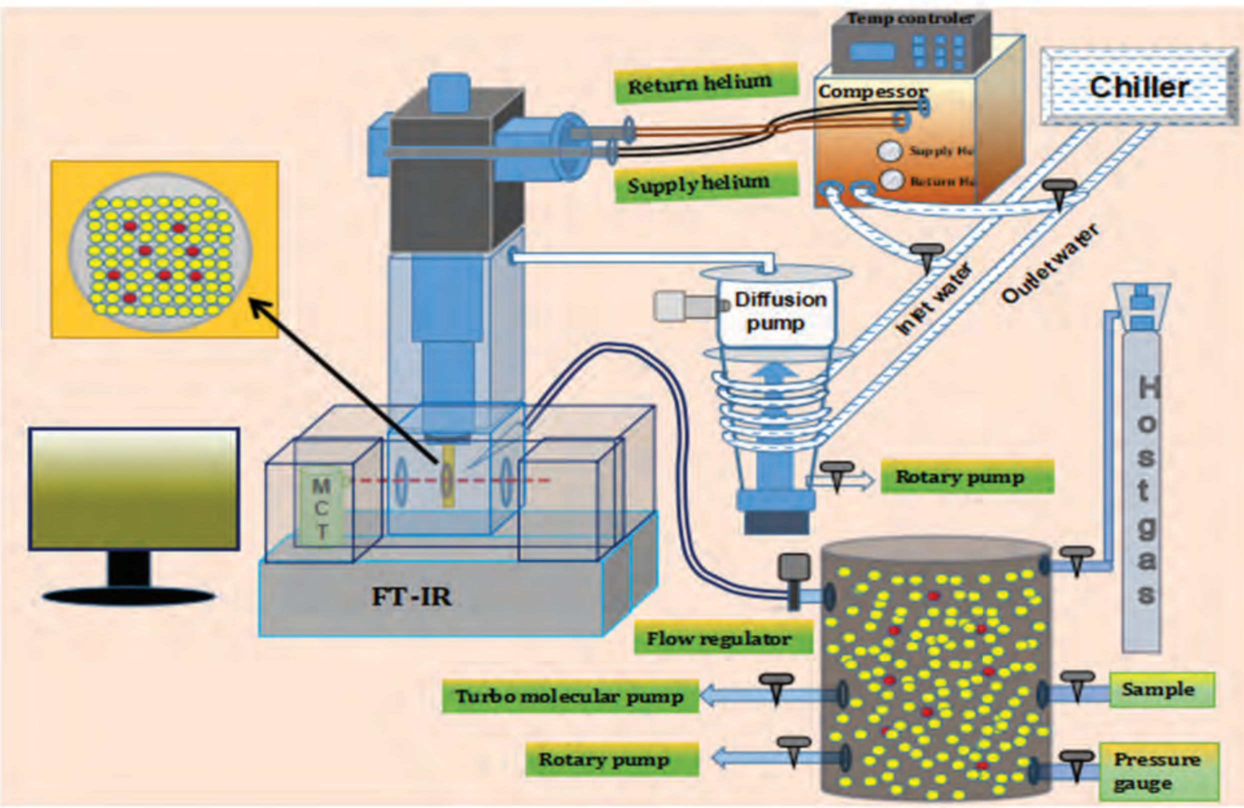

Fig. 1: The schematic of matrix isolation setup

conformational differences determine molecular recognition and drug action. In materials science, conformational flexibility influences packing and mechanical properties. Even human vision originates from photoisomerization of retinal, where a tiny conformational change transforms light into visual perception. Thus, a simple molecular twist can determine whether a material bends or breaks, whether a drug heals or fails, and whether a reaction proceeds or stops.

Matrix isolation infrared spectroscopy has emerged as one of the most powerful techniques for investigating cold-isolated molecules. In this technique, molecules are trapped in inert cryogenic matrices such as Ne, Ar, Kr, Xe, or N_2 at temperatures close to 10 K, minimizing intermolecular interactions and suppressing thermal broadening. Among all spectroscopic probes, infrared spectroscopy stands out because it directly captures vibrational fingerprints highly sensitive to molecular structure and environment. Together, matrix isolation and infrared spectroscopy provide a uniquely powerful molecular window for isolating, identifying, and understanding molecules that often remain hidden in the bulk phase. The schematic of matrix isolation setup is shown in Fig. 1.

The strength of matrix isolation spectroscopy becomes evident when infrared spectra recorded under bulk and cryogenic isolated conditions are compared. The infrared spectra of trimethyl phosphate recorded as liquid and solid film exhibit broad unresolved features due to intermolecular interactions and thermal effects, whereas the spectrum recorded in Xe matrix at 12 K displays sharp and highly resolved bands corresponding to isolated molecular species (Fig. 2). Similarly, rotational congestion observed in the gas-phase spectrum of HCl disappears upon matrix isolation in N_2, resulting in simplified vibrational features with enhanced resolution.

To investigate conformational populations experimentally, room-temperature effusive and heated nozzles, and supersonic molecular beam expansions are generally employed. Supersonic expansion rapidly cools molecules through adiabatic expansion, producing low-temperature equilibrium conformational populations before matrix deposition, whereas effusive deposition preserves room-temperature vapor-phase populations. Matrix isolation exhibits site-splitting, where molecules trapped in slightly different matrix environments produce multiple closely spaced spectral features. Annealing softens the rigid matrix environment and enables molecular diffusion, conformational relaxation, and aggregation.

Detailed studies on trimethyl phosphate and trimethyl phosphite in our laboratory demonstrate the remarkable power of matrix isolation spectroscopy for conformational analysis. In trimethyl phosphate isolated in N_2 matrix, two experimentally relevant conformers, "Gauche" and "Trans," are observed. Annealing show that room-temperature conformational populations become frozen in the matrix, whereas supersonic expansion favors low-temperature equilibrium populations. Trimethyl phosphite exhibits a very different conformational landscape because of the absence of the phosphoryl group. Here, the "Trans" conformer represents the ground state, while the "Gauche" conformer becomes energetically unfavorable

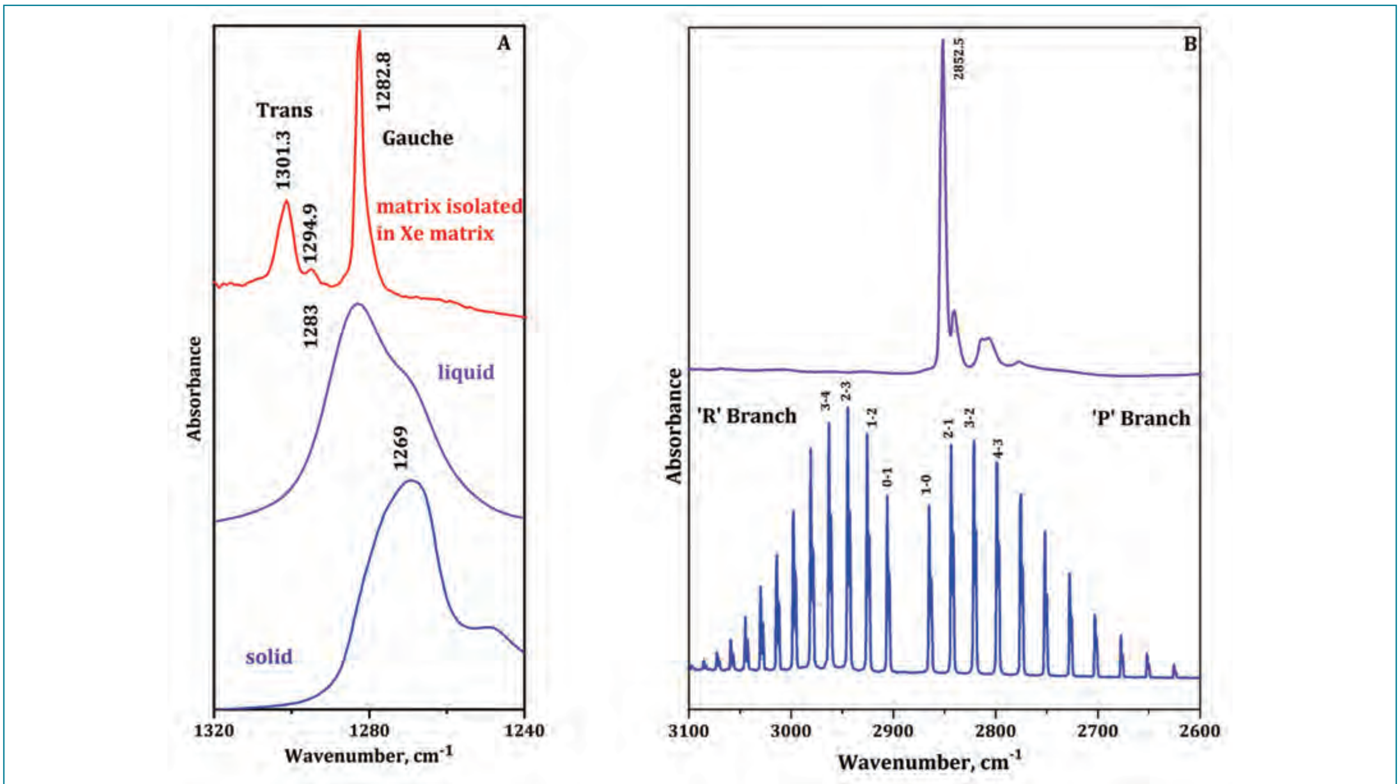

Fig. 2: Infrared spectra of A) trimethyl phosphate as solid film, liquid and under isolated condition in Xe matrix at 12 K. B) Infrared spectra of HCl in gas phase and under isolated conditions in N_2 matrix at 12 K

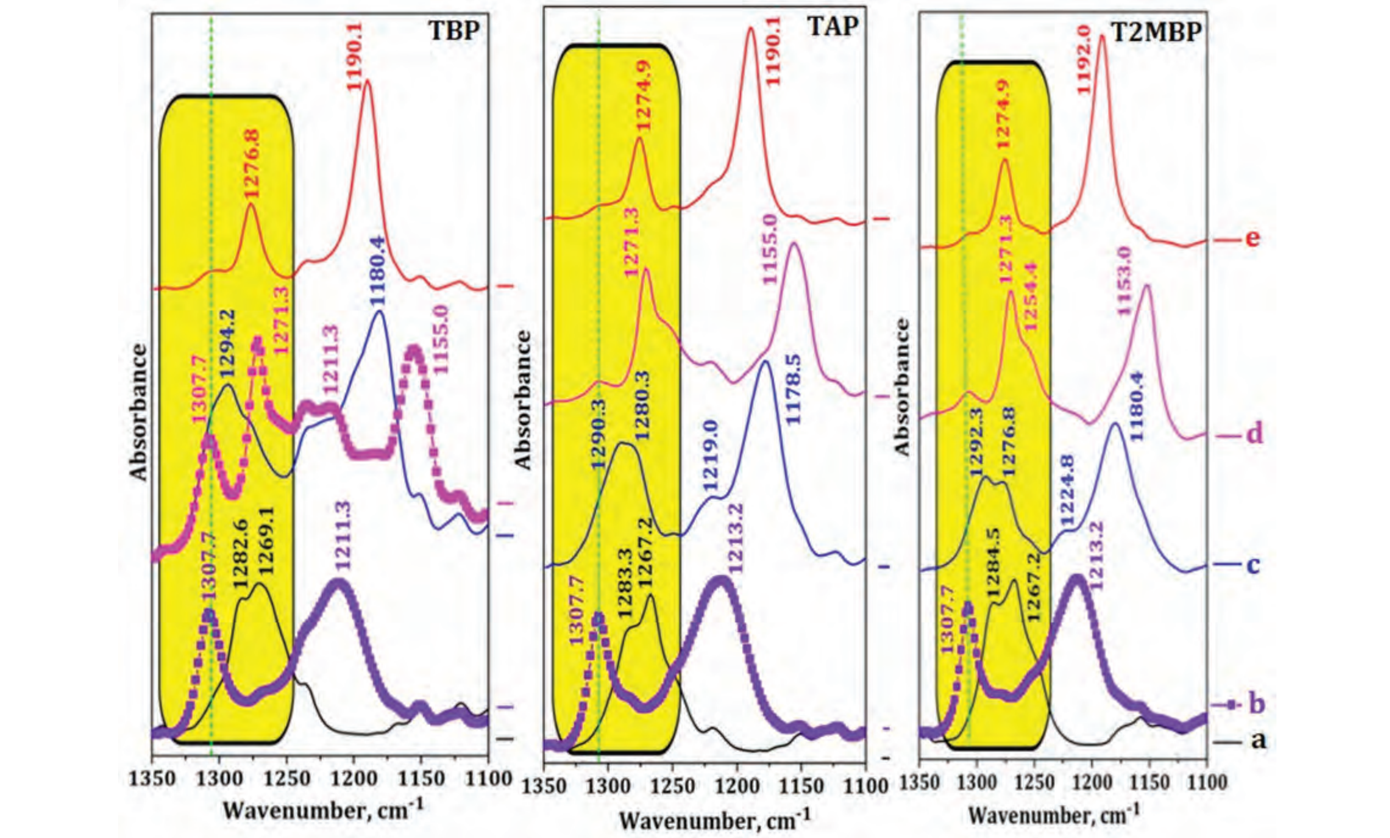

Fig. 3: Infrared spectra of metal loaded phosphates at MOC/LOC. a) 30% extractant in *n*-DD, b) 30% extractant in *n*-DD with 5 M HNO_3, 30% extractant in *n*-DD with c) LOC of $Th(NO_3)_4$, d) LOC/MOC of $Pu(NO_3)_4$ and e) MOC of $UO_2(NO_3)_2$. The aqueous equilibrium phase HNO_3 concentration was maintained at 2.7 M for Th(IV) and 5 M for U(VI), Pu(IV) complexes

due to absence of d–p orbital mixing.

Photo-oxidation experiments performed by introducing oxygen dopants into N_2 matrix containing trimethyl phosphite generate the corresponding phosphate species *in situ*. Interestingly, the resulting conformational population deviates strongly from equilibrium conditions, exhibiting enrichment of the "Trans" conformer. These observations demonstrate the importance of the matrix cage effect, where surrounding matrix molecules preserve non-equilibrium conformational distributions during chemical transformations. The influence of matrix surroundings becomes evident in Ar and Kr matrices, where annealing gradually converts the "Gauche" conformer into the more stable "Trans" conformer for Trimethyl phosphate.

The conformational behavior of tri-*n*-butyl phosphate (TBP) and branched analogues such as tri-*amyl*-phosphate (TAP) and tris-*2-methyl-butyl*-phosphate (T2MBP) further establishes the intimate relationship between molecular structure and macroscopic behavior. Solution-phase infrared spectroscopic investigations involving U, Th, and Pu nitrate systems reveal that increasing metal nitrate loading gradually increases the polarity of the organic phase (Fig. 3). Near Limiting Organic Concentrations (LOC), enrichment of the higher dipole "Trans" conformer is observed, identified through enhancement of the infrared band near 1290 cm^{-1}. The increasing "Trans" population creates polarity mismatch between extractant and diluent, ultimately driving third phase formation. Importantly, this conformational transition occurs before actual phase splitting, establishing enrichment of the "Trans" conformer as a molecular-level pre-monitor for impending third phase formation. This enrichment was found to be completely absent in scenarios where third phase does not form: U with all phosphates, Pu with TAP and T2MBP at Maximum Organic Concentration (MOC). These findings reveal that conformations are not passive structural details but active molecular triggers governing polarity, interactions, and macroscopic chemical behavior.

These investigations collectively demonstrate that molecules are dynamic systems whose shapes govern their behavior and function. Matrix isolation infrared spectroscopy provides a uniquely powerful approach for probing this hidden molecular landscape by minimizing thermal motion and intermolecular perturbations. The studies on conformations, photo-oxidation, molecular beam deposition, and structure–activity relationships clearly reveal that even the smallest molecular rearrangements can profoundly influence stability, reactivity, interactions, and functionality. Ultimately, the chemistry of cold-isolated molecules highlights one of the most important truths of molecular science: invisible molecular motions can lead to visible consequences across chemistry, biology, materials science, and life itself.

Shri PRAMOD KUMAR CHAURASIA
Fast Reactor Technology Group
Indira Gandhi Centre for Atomic Research
Kalpakkam, Tamil Nadu, India

LECTURE SERIES

IRRADIATION OF REACTOR MATERIALS IN FAST BREEDER TEST REACTOR (FBTR)

Fast Breeder Test Reactor (FBTR) at Kalpakkam, India is a sodium cooled fast reactor with neutron flux level of the order of 10^{15} n/(cm^2 s) and temperature of coolant in the range of 380–520 °C, which is being used for the development of fuel, structural and shielding materials required for Indian Fast Reactor Program. It is also used for the production of radioisotopes. The knowledge about the behaviour of fuel and structural materials in hostile environment of reactor core is very important for design, operation and safety of fast reactors, by carrying out the irradiation experiments.

Innovative Design, Engineering And Synthesis (IDEAS) Section has specialized in design and planning of irradiation experiments in FBTR. Substantial developmental efforts are made to carry out the irradiation experiments. Out-of-pile laboratory experiments are also carried out in IDEAS, to give proper shape to the in-pile experiments. Indigenous capability and expertise have been developed to carry out a variety of irradiation experiments in FBTR. Irradiation experiments are experiments that are carried out under intense neutron environment of a nuclear reactor simulating the main experimental parameters in order to assess the irradiation performance behaviour of the materials under investigation. Accelerated irradiation experiments can also be planned in FBTR on thermal reactor core structural materials to determine their behaviour, in a short period of time. Irradiation experiments can be classified according to type of the materials to be irradiated such as (i) Fuel irradiation experiments, (ii) Structural material irradiation experiments, (iii) Irradiation experiments for the production of isotopes, (iv) Irradiation experiments on non-core materials etc. Irradiation of reactor materials that have been carried out in FBTR are: (i) Irradiation of experimental fuel pins with Mark-I carbide fuel of FBTR to determine the beginning of life behaviour of the fuel, (ii) Irradiation experiment to determine the irradiation creep rate of pressure tube materials (Zircaloy-2 and Zr-2.5% Nb alloy) of Indian Pressurised Heavy Water Reactors

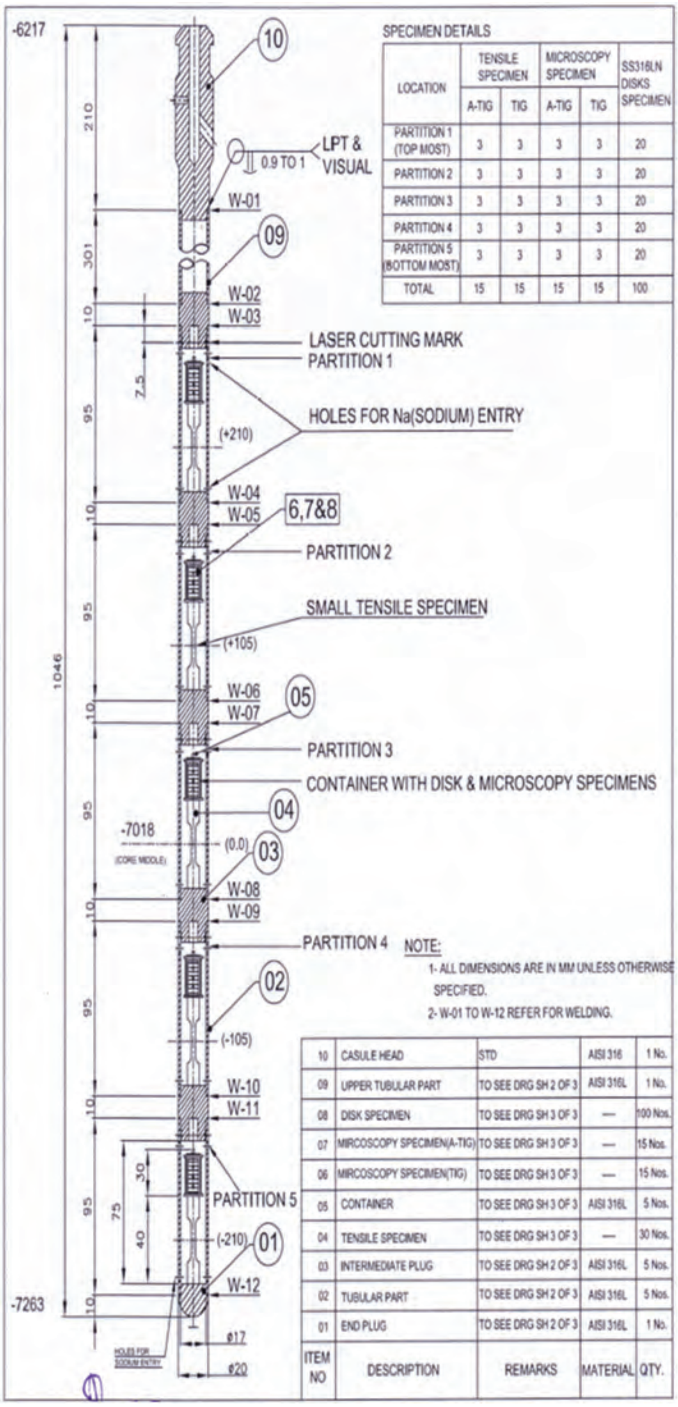

Fig. 1: Sketch of a typical irradiation capsule

(PHWR), (iii) Experiment to determine the irradiation hardening behavior of FBTR grid plate material & to assess the remaining life of reactor, (iv) Experiment to determine the irradiation creep behaviour of indigenously developed D9 alloy, (v) Irradiation of a single PFBR fuel pin to determine the initial gap closure behavior, (vi) Irradiation of sodium bonded metal fuel pins of different compositions such as ternary fuel-1 (23%Pu-19%EU-6%Zr), ternary fuel-2 (19%Pu-U-6%Zr), binary fuel (14.8%EU-6%Zr) and natural uranium-6%Zr etc. to determine its behavior & to establish its reprocessing route, (vii) Irradiation of TRISO coated particles of fuel surrogate material, for the use in Compact High Temperature Reactor (CHTR), BARC; (viii) Irradiation of advanced core structural materials such as D9I (other name IFAC-1), Reduced Activation Ferritic-Martensitic (RAFM) steel, Oxide-Dispersion-Strengthened (ODS) alloy etc., (ix) Irradiation of A-TIG weld samples to understand its mechanical & microstructural properties, (x) Irradiation of nickel specimens to understand the trapping behavior of it for the radionuclide (Mn-54), (xi) Irradiation of ferro-boron (FeB), which is a potential shielding material for in-vessel applications, (xii) Irradiation of Tungsten Carbide (WC) pellets, which is a potential lower axial shield material in fuel subassemblies for reducing the fluence on the grid plate, (xiii) Irradiation of yttrium oxide (yttria) pellets for production of Strontium-89 radioisotope for medical applications; and (xiv) Irradiation of sintered pellets of Strontium Sulphate ($SrSO_4$) as target material for the production of Phosphorus-32 (^{32}P) isotope, which is having several applications in pharmaceutical industry as well as in microbiology fields. Samples to be irradiated in reactor core, are contained in the irradiation capsule, which in turn can be loaded in special sub-assembly and can be locked in it using bayonet type locking arrangement. After irradiation in FBTR core, the irradiation capsules & the irradiated samples are retrieved in the hot cells of Radio metallurgy Laboratory (RML) and post irradiation examinations are carried out on the irradiated samples. Sketch of a Typical Irradiation capsule is shown in Fig. 1, specimens along with the components of a typical irradiation capsule is shown in Fig. 2, assembled irradiation capsule is shown in Fig. 3 and the special sub-assembly is shown in Fig. 4.

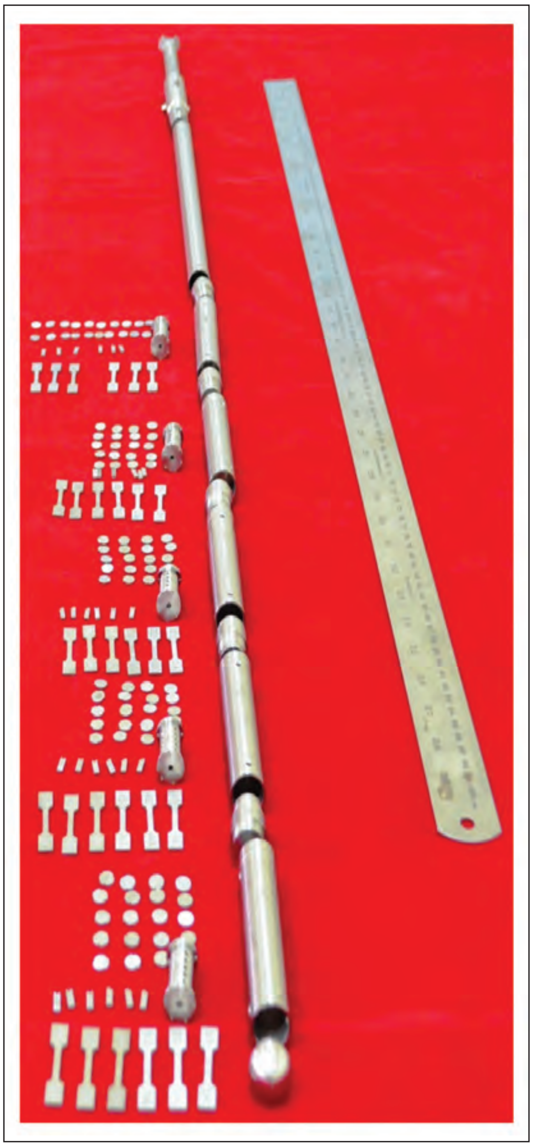

Fig. 2: Specimens along with the components of a typical irradiation capsule

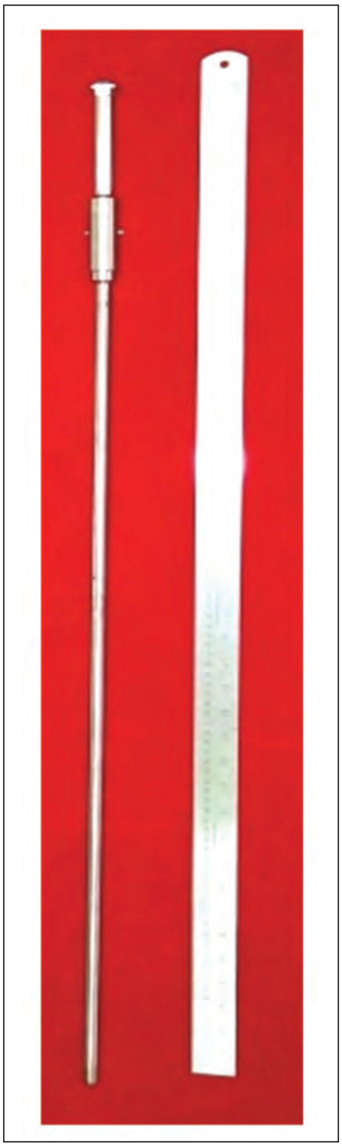

Fig. 3: Assembled irradiation capsule

Fig. 4: The special sub-assembly loaded with irradiation capsule

Dr. PRAMOD KUMAR SHARMA
Reactor Design Group
Indira Gandhi Centre for Atomic Research
Kalpakkam, Tamil Nadu, India

LECTURE SERIES

Residual Risk in Nuclear Safety: Towards a Concept of Inherent Core Damage Frequency

Probabilistic Safety Assessment (PSA) has evolved into one of the most important tools for evaluating the safety of nuclear power plants. By systematically modelling initiating events, equipment failures, human actions and accident progression, PSA provides quantitative measures of plant risk, the most widely used being the Core Damage Frequency (CDF). Over the past several decades, continuous improvements in reactor design, redundancy, diversity, passive safety features and operational practices have contributed to significant reductions in estimated CDF values. Nevertheless, it is widely recognized that absolute safety is unattainable and that some degree of residual risk always remains.

The concept of residual risk is not unique to the nuclear industry. Major engineering programmes, including space missions, aircraft operations and large industrial facilities, routinely acknowledge that a finite level of risk persists even after extensive safety measures have been implemented. The success of a system therefore depends not only on reducing risk but also on understanding the nature and magnitude of the risk that remains.

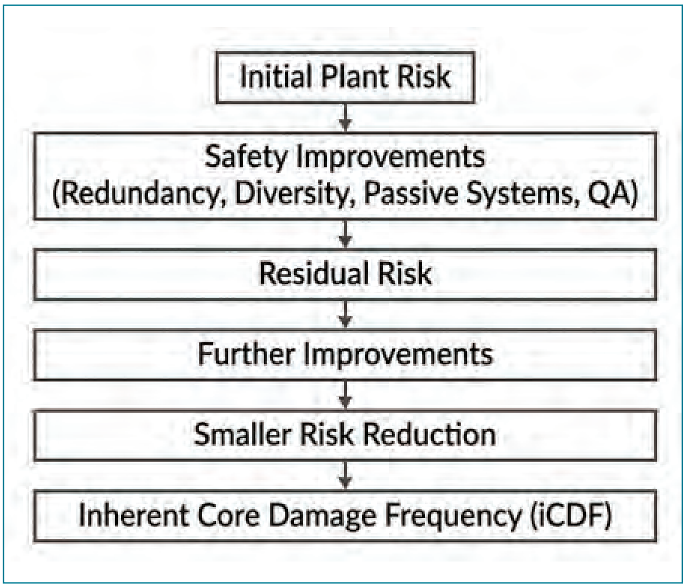

Fig. 1: Schematic representation of diminishing returns in risk reduction eventually leading to the Inherent Core Damage Frequency (iCDF) plateau

This observation motivated an investigation into a more fundamental question: Is there a practical lower limit to risk reduction? While residual risk describes the risk remaining after implementation of a particular set of safety provisions, it does not indicate whether additional improvements can continue reducing risk indefinitely. The proposed concept of Inherent Core Damage Frequency (iCDF) attempts to address this question by defining a practical lower bound of achievable risk under prevailing physical, engineering and epistemic constraints (Fig. 1).

The idea emerged from studies carried out in the area of Seismic Probabilistic Safety Assessment (SPSA) for Fast Breeder Reactor systems. SPSA combines information on seismic hazard, component fragility and plant response to estimate the contribution of earthquake-induced failures to overall plant risk. During investigations involving system reduction techniques, it was observed that the calculated CDF did not approach zero even when the analysis was progressively simplified to retain only the dominant contributors to seismic risk. Instead, a finite minimum value persisted (Fig. 2).

This behaviour can be attributed to several factors. Seismic hazards cannot be eliminated from the environment. Structural and equipment fragilities can be improved but cannot be reduced to zero. Common-cause effects arising from a common seismic excitation remain important even in highly redundant systems. In addition, modelling uncertainties and the possibility

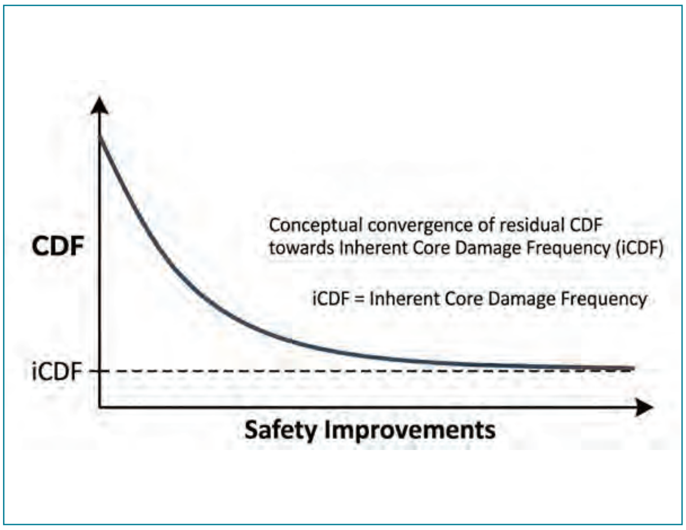

Fig. 2: Conceptual convergence of residual CDF towards Inherent Core Damage Frequency (iCDF) with successive safety improvements

of rare extreme events continue to contribute to risk. Together, these factors suggest the existence of a practical risk floor that cannot be completely eliminated through conventional design enhancements.

To explore this possibility, a case study was performed using the Level-1 Seismic PSA model of the Prototype Fast Breeder Reactor (PFBR). Through systematic reduction of accident sequences and identification of dominant contributors, a minimum achievable CDF of approximately 4.54×10^{-6} per reactor-year was estimated. This value was compared with the calculated plant CDF of approximately 6.80×10^{-6} per reactor-year. The relatively small difference between these values indicates that substantial risk reductions have already been achieved and that future improvements may yield progressively smaller gains in safety.

The proposed iCDF concept may therefore be viewed as a quantitative manifestation of inherent risk expressed in terms of CDF. Unlike residual risk, which depends on the specific design and safety provisions under consideration, iCDF represents the practical lower bound towards which residual CDF may converge as additional safety measures are implemented. In this sense, iCDF is not intended to replace existing PSA metrics but rather to complement them by providing insight into the ultimate limits of risk reduction.

The concept may have several potential applications in future safety assessments. It can assist in identifying situations where additional safety enhancements produce diminishing reductions in risk, thereby supporting more effective allocation of resources. It may also contribute to discussions on risk-informed regulation, optimization of safety investments and prioritization of plant upgrades. Furthermore, the concept provides a framework for comparing different reactor technologies in terms of their achievable minimum risk levels.

The development of PSA methodologies has historically influenced many other disciplines, including aerospace engineering, chemical process safety, reliability engineering, finance and medicine. Concepts such as fault tree analysis, event tree analysis and quantitative risk assessment, originally developed for nuclear applications, have found widespread adoption in these fields. The proposed concept of iCDF represents a further contribution to the continuing evolution of risk science.

Although additional studies involving different reactor types and external hazards are required, the concept introduces a new perspective on nuclear safety by focusing attention not only on risk reduction but also on the practical limits of achievable risk. Understanding these limits may become increasingly important as future reactor designs seek ever lower levels of risk while maintaining economic viability and operational efficiency.

Shri G. YATHISH KUMAR
Materials Chemistry & Metal Fuel Cycle Group
Indira Gandhi Centre for Atomic Research
Kalpakkam, Tamil Nadu, India

LECTURE SERIES

Process & Instrumentation for Metal Fuel Fabrication

Sodium bonded metallic fuel pins containing U-19wt.%Pu-6wt.%Zr ternary alloy as fuel slug and U-6wt.%Zr binary alloy as blanket slug in T91 clad are being developed for future fast breeder reactors in India. Sodium bonded metallic fuel containing uranium–plutonium–zirconium (U–Pu–Zr) alloy having high fissile atom density & high thermal conductivity gives significant advantages like high breeding ratio, low doubling time, inherent safety, proliferation resistant over conventional ceramic fuels. Metallic fuels face challenges like swelling, fission gas release, and cladding interaction during high burnup. These can be mitigated through alloy optimization, sodium bonding, and advanced cladding materials.

A dedicated facility at MCFMCG, IGCAR was set up to fabricate metallic fuel pins for irradiation in FBTR. Process flow sheet for metal fuel fabrication is described in Fig. 1. The process begins with injection casting of Uranium–Plutonium–Zirconium alloy fuel slugs and Uranium–Zirconium alloy blanket slug in quartz moulds under controlled atmosphere. After casting, the slugs are demoulded, end sheared to required dimensions, and subjected to metrology for physical characterization. Qualified slugs are then loaded into bottom end closed T91 clad tubes leaving a small annular gap between fuel and cladding. This gap is filled with liquid sodium, which provides a thermal bond, enhances heat transfer, and accommodates fuel swelling during irradiation. Further the clad tube top end is sealed with top end plug by welding, followed by post weld heat treatment and sodium bonding process.

The fabrication of metal fuel pins is a multi-stage process carried out inside interconnected glove box trains, where each stage is tightly linked and supported by automated instrumentation.

Injection Casting forms the starting point, where U–Zr alloy slugs are produced (Fig. 2). Because fluid properties remain uncertain and solidification shrinkage affects casting quality, especially with the fuel rod L/D ratio, modular process control system was designed. A PLC–SCADA based automated system integrates vacuum, pressure, temperature, motion mechanisms with safe handling of radioactive materials. Control system allows parameters such as melt temperature, injection pressure, and mould pre-heating to be tuned and validated, with reliability ensured through modular logic, interlocks, trip logics, and a robust user interface.

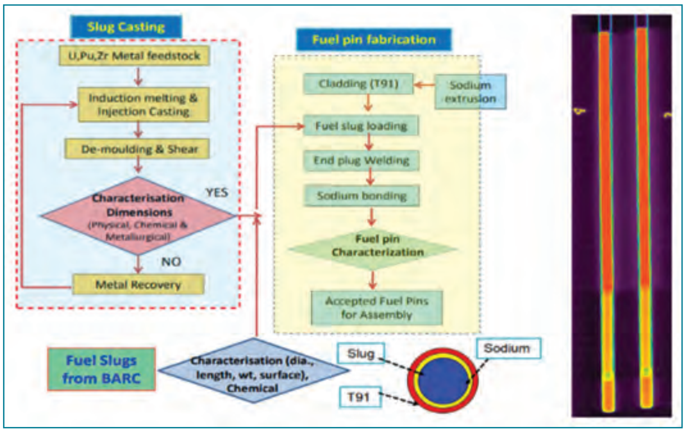

Fig. 1: Process flow sheet for metal fuel fabrication

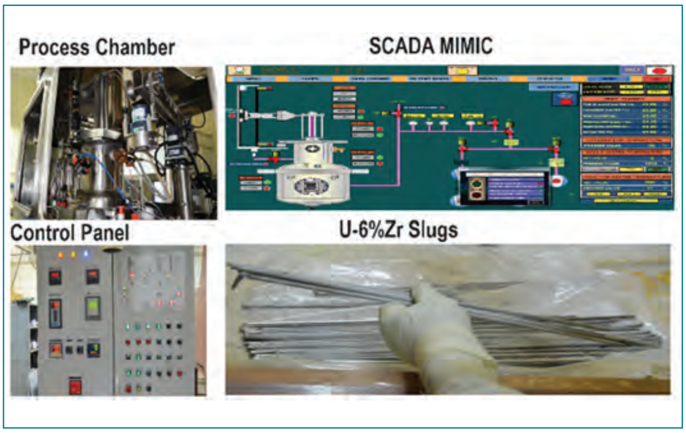

Fig. 2: Process of injection casting

Once slugs are cast, Slug Metrology ensures dimensional and quality checks. An automated bench with sensors, motors, and position switches measures weight, diameter, and length, while eddy current testing supported by NDED, MMG detects surface defects. A servo motor drive moves slugs across all stages, and PLC–SCADA integration automates inspection, validation, and data collection. Each cycle is logged with batch ID and time stamps. In SCADA UI tolerance limits decide acceptance or rejection of fuel slugs. Data is stored for retrieval and post-cast analysis System is installed with probes inside glove boxes and signal conditioning electronics outside glove box to reduce radiation exposure (Fig. 3).

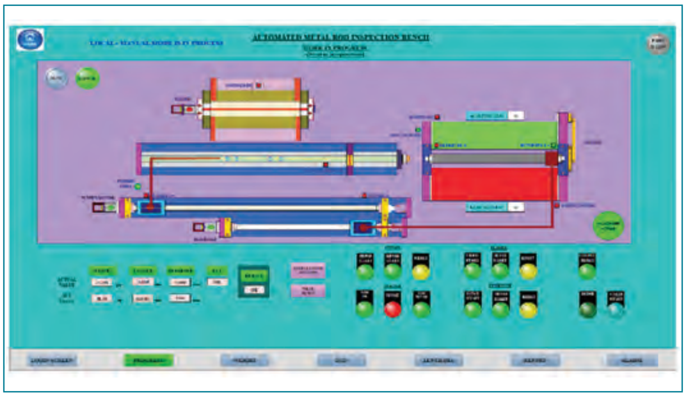

Fig. 3: Slug metrology SCADA

To complement metrology, a Vision System adds advanced surface inspection. Using a line-scanner camera and laser 3D profilometer mounted on a linear servo drive with rotary grippers, the rod surface is scanned along its length and rotated through 360°. Real-time images are stitched into 3D reconstructions using Halcon MV libraries. PLC-based trigger control synchronizes the vision system with motion drives, and preset defect thresholds guide acceptance or rejection, with images and data archived for future analysis.

Following inspection, Fuel Pin Welding is carried out by PLC–HMI based control scheme. Operators define timing sequences on the HMI and the PLC executes synchronized welding and motor actuation cycles. Sensors and interlocks ensure safe operation, while welding data is logged for traceability.

Next, Sodium Bonding improves interface quality between sodium and fuel slugs. Fuel pins are heated to 773 K using 1.5 kW mineral-insulated cartridge heaters. Thyristor modules and PLC–HMI controllers manage heating and cooling profiles, while multipoint N-type thermocouples provide multi-zone monitoring. Continuous data logging via Modbus over TCP/IP supports process optimization and quality control.

All these stages depend on Allied Glove Box Systems, which provide inert, leak-tight enclosures (<0.05% volume leakage per hour) with HEPA filtration. A PLC–HMI pressure control system maintains stability, containment and for contamination prevention, with set points typically between −20 and −40 mm. Automated purging modules evacuate and refill gas to reduce impurities to ~1000 ppm, while leak testing follows ISO 10648-2 standards using pressure change and oxygen concentration methods. Regeneration systems operate in auto or manual modes by HMI selection of heating, purging, vacuum, and cooling cycles with PID-controlled heaters and angle seat valves. Redundant towers run in parallel to ensure continuous purification of glove box pairs, and the parameters like pressure, oxygen, moisture which has greater impact on various properties of the fuel pin fabrication stages are logged. Purification column regeneration parameter provides the insight into column saturation level and load on each glove boxes for quality control and assurance in fuel pin fabrication (Fig. 4).

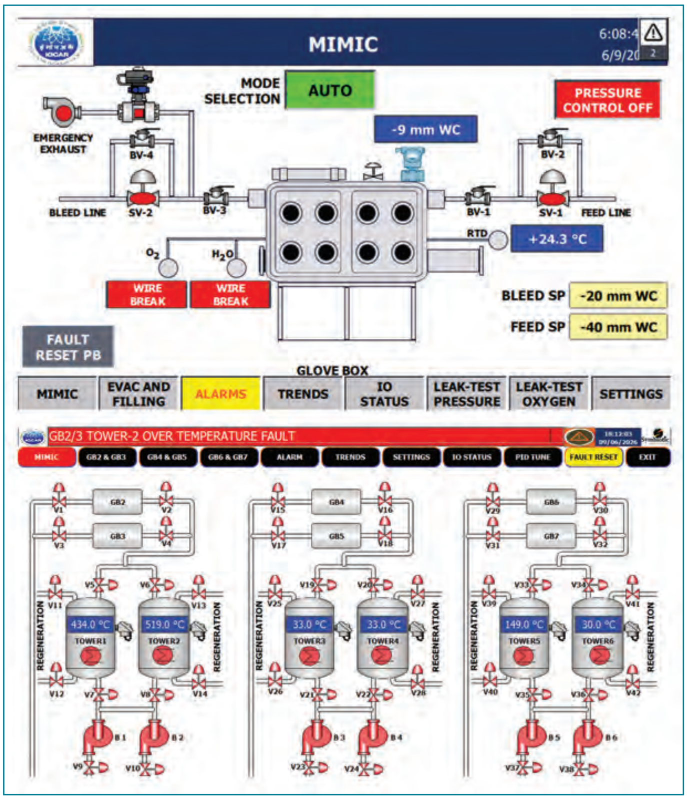

Fig. 4: HMI of GB pressure control and recirculation

Finally, the entire glove box train operates under a hybrid control architecture. Centralized monitoring ensures data integrity, traceability, and analytics, while localized control avoids common-mode failures and supporting modular development. This balance of centralized data management with independent system execution ensures reliability, flexibility, and quicker implementation across the fabrication line.

Technology Week Celebrations at Visvesvaraya Industrial and Technological Museum (VITM)

May 8th–11th 2026

Indira Gandhi Centre for Atomic Research (IGCAR), Kalpakkam, organised a four-day public awareness programme themed "Atoms in the Service of the Nation" at the Visvesvaraya Industrial and Technological Museum (VITM), Bengaluru, from 8th to 11th May 2026. The event, held in collaboration with VITM (a unit of the National Council of Science Museums, Ministry of Culture), aimed to engage school and college students from the southern states.

The exhibition was formally inaugurated by Shri Sreekumar G. Pillai, Director of Indira Gandhi Centre for Atomic Research. He also delivered the inaugural address on the topic "**Energy Security through India's Three-Stage Nuclear Power Programme.**" The lecture highlighted India's long-term vision for achieving sustainable energy security through the strategic utilisation of nuclear power resources. A total of **220 students** and **41 volunteers** benefitted from the inaugural session and lecture.

The four day exhibition witnessed the active participation of 41 volunteers, who played a significant role in the successful conduct of the programme. The volunteers assisted in explaining and demonstrating various stalls and exhibits to visitors, helping them understand the concepts and applications of nuclear science and atomic energy. They also actively engaged visiting children in themed educational and interactive activities conducted throughout the exhibition.

The exhibition received an overwhelming response from visitors during all four days. The day wise visitor statistics are as follows:

08 May 2026 – 2,269 visitors
09 May 2026 – 4,696 visitors
10 May 2026 – 4,425 visitors
11 May 2026 – 1,846 visitors

The exhibition concluded successfully on 11 May 2026 .

Theme Meeting on Structural Materials and Associated Technologies for Application in Nuclear Industry (SMATAN-2026) - May 21st & 22nd, 2026

A two-day Theme Meeting on "Structural Materials and Associated Technologies for Application in Nuclear Industry (SMATAN-2026)" was jointly organized by Indira Gandhi Centre for Atomic Research (IGCAR), Kalpakkam, the Board of Research in Nuclear Sciences (BRNS), Mumbai and the Kalpakkam Chapter of the Indian Institute of Metals (IIM) at IGCAR, Kalpakkam, on 21–22 May 2026.

The technical sessions featured invited lectures by distinguished scientists, engineers, academicians, and industry professionals, covering a wide spectrum of current and emerging topics. This included hydride embrittlement and its mitigation in zirconium alloys, extraction of critical metals, laser-based additive manufacturing, advanced joining techniques, development of core structural and cladding materials for fast reactors, and combinatorial strategies for accelerated materials discovery.

The presentations also delved into the design and fabrication of fast reactor components, next-generation Cr–Mo steels tailored for nuclear service, and the growing role of Artificial Intelligence and Machine Learning in manufacturing and joining processes offering a comprehensive overview of recent progress in structural materials and related technologies for nuclear applications. In addition, the meeting provided a vibrant platform for early-career researchers to interact directly with leading experts, facilitating knowledge exchange and strengthening the connections between fundamental materials research, technological innovation, and engineering deployment in support of advanced nuclear energy systems.

Reported by
Dr. A. Nagesha
Head/MMD

Theme Meeting on Radiation based Non-destructive Assessment of Materials (RNAM 2026)

May 25th, 2026

A half day theme meeting on Radiation Based Nondestructive Assessment of Materials (RNAM 2026) was conducted on 25th May 2026 at the NDED Auditorium, IGCAR. The event was organised by the Indira Gandhi Centre for Atomic Research (IGCAR) in association with the Indian Society for Nondestructive Testing (ISNT), Kalpakkam Chapter.

The technical proceedings commenced with opening remarks by **Dr. Anish Kumar**, Director, MMG & MSG, IGCAR, who highlighted the significance of high energy radiation techniques in advancing nondestructive evaluation (NDE) capabilities for critical materials and components. Eminent experts from BARC, IGCAR, RRCAT, and VSSC delivered lectures covering state of the art radiation based NDE methodologies. The talks spanned a wide spectrum of high energy radiation applications, including: Synchrotron based techniques for strategic material assessment, Industrial X ray tomography for internal defect characterization, LINAC based NDE applications for space components, X ray diffraction methods for microstructural evaluation and Infrared thermography and other radiation based approaches for rapid nondestructive testing. These sessions provided deep insights into emerging trends, indigenous developments, and cross disciplinary applications of radiation assisted NDE.

The meeting witnessed active participation of sixty delegates from different groups of IGCAR. The interactions and discussions reflected the strong interest of the scientific community in leveraging radiation based techniques for advanced material assessment. The program concluded with remarks by Dr. S. Thirunavukkarasu, Head, EMSIS, NDED, IGCAR, who summarised the key takeaways.

Reported by
Dr. S. Thirunavukkarasu
Head, EMSIS, NDED

Theme Meeting on Novel Materials: Strongly Correlated, Functional and Quantum Materials

May 26th, 2026

A one-day Theme Meeting on Novel Materials: Strongly Correlated, Functional and Quantum Materials was organized by Materials Science Group, IGCAR along with MRSI, Kalpakkam chapter on 26th May, 2026.

Theme meeting focused on novel materials such as strongly correlated, functional, and quantum materials which are at the forefront of modern materials science and condensed matter physics and are active areas of research at MSG. Inaugurated by Director, IGCAR, the event was attended by 85 delegates, including employees and students from IGCAR and other DAE units at Kalpakkam. The program featured six invited talks and three expert lectures delivered by eminent speakers, highlighted by **Prof. Chandrabhas Narayana** from JNCASR, who spoke on detecting pressure-induced topological transitions using Raman spectroscopy. The invited sessions spanned a diverse range of topics, including strongly spin-polarized Heusler alloys, super-extensive charging power in the absence of global operations, optical non-linearity in TiO_2 systems, and the development of quantum technology using superconducting qubits.

Additionally, the expert talks detailed advanced research on the physical properties of the Chromium-telluride system via Cr-self intercalation, confined conduction channels near a metal-insulator transition, and the Quantum Spin Hall state in InAs/GaSb quantum wells. The event concluded with closing remarks from **Dr. Awadhesh Mani**, then Head, Condensed Matter Physics Division (CMPD), MSG.

Awards, Honours and Recognitions

R. Priya, SO/F, CSTD received the IIM Kalpakkam chapter Best Journal Paper Award (General category) for the paper entitled "Corrosion behaviour of Ti-grade2 dissolver material in nitric acid containing fluoride ions", Authored by R. Priya, K. Kaliraj and S. Ningshen, Journal of Nuclear Materials 612 (2025) 155833.

R. Duraipandi, SRF, received the IIM Kalpakkam chapter Best Journal Paper (Young researcher category) for the paper titled "Influence of load ratio on fatigue crack growth behavior of SS316L(N) using a two parameter model", International Journal of Fatigue 193 (2025) 108778.

V. Athulya, SRF, received the IIM Kalpakkam chapter Best Journal Paper (Young researcher category) for the paper titled "Durable Ce-Ni myristate superhydrophobic coating on steel with corrosion and biofouling resistance", Authored by V. Athulya, S.C. Vanithakumari, C. Thinaharan, S. Sofia, A. Ravi Shankar and S. Ningshen, Materials Chemistry and Physics 347 (2026) 131450.

Akshyata Kirtania, SRF, received the IIM Kalpakkam chapter Best Paper Award (Young researcher category) for the paper titled "High temperature corrosion evaluation of SS 316L in CeCl3-LiCl-KCl molten salt using electrochemical techniques", Authored by Akshyata Kirtania, Ch. Jagadeeswara Rao, S. Ningshen, Corrosion Science 259 (2025) 113483.

Akshyata Kirtania, SRF, received the Second Prize for the Poster Presentation for the paper entitled "High temperature corrosion evaluation of SS 316L in CeCl3-LiCl-KCl molten salt using electrochemical techniques", Authored by Akshyata Kirtania, Ch. Jagadeeswara Rao, S. Ningshen, HBNI Technical Meet for Research Scholars, IGCAR, Kalpakkam, 15th May 2026.

A.D. Hemne, JRF, received the Second Prize for the Oral Presentation for the paper entitled "Tribocorrosion performance of titanium for nuclear fuel reprocessing rotary dissolver application", HBNI Technical Meet for Research Scholars, IGCAR, Kalpakkam, 15th May 2026.

K. Kaliraj, AFM, CSTD received the Second Prize for the Poster Presentation for the paper entitled "Corrosion performance of alumina-coated titanium modified 316L (D9-I) SS in molten lead-bismuth eutectic coolants for generation-IV nuclear reactor", National Technology Day (NTD-2026), IGCAR, 14th May 2026.

Dr. S. Ningshen, Dr. E. Vetrivendan and Dr. C. Anushree were awarded a Certificate of Appreciation by IGCAR in recognition of significant contributions to the installation, testing, and commissioning of the Cu-Cl based Hydrogen Production System at the Fast Breeder Test Reactor (FBTR).

Dr. S. Ningshen, Head, CSTD received the Springer Nature Editor of Distinction Awards – 2026 - Editorial Contribution Award 2026 and Author Service Award 2026.

Dr. Ram Kumar Maity, Shri Amit Kumar Chauhan, Shri M. Rajendrakumar, and Dr. K. Natesan received the Best Paper Presentation Award at IICHE CHEMCON 2025, paper titled: "An efficient hybrid model of intermediate heat exchanger of a sodium cooled nuclear fast reactor", Annamalainagar, 27th–30th December 2025.

Dr. Amit Patel, IGCAR Kalpakkam have been elected to the Executive Committee (EC) of the Indian Aerosol Science and Technology Association (IASTA) for the next 3 years (2026–2028).

Shri P. Ramesh, SA/F and Shri M. Mohamed Amjath, AFM of QAD, received the Second Prize and a Certificate of Appreciation, poster titled: "Development of an instrument for aided visual examination at inaccessible areas in pipelines", National Technology Day (NTD-2026), IGCAR, 14th May 2026.

Shri V. Prabakaran, AFM received the First Prize for the Poster Presentation for the paper entitled "Radiometry testing of lead bricks for shielding primary sodium and cover gas pipelines at PFBR site", National Technology Day (NTD-2026), IGCAR, 14th May 2026.

Shri D. Suresh, AFM and Shri P. Ettiyappan, T/D, QAD, received the Second Prize in the Best Exhibit, "Improving productivity using dedicated fixture for radiography testing of onsite pipe weld joints", National Technology Day (NTD-2026), IGCAR, 14th May 2026.

Bio-diversity @ DAE Campus, Kalpakkam

Editorial Committee Members

Little Egret

Little Egret is the smallest egret and has a black bill, black legs and yellow feet. In the breeding season, the facial skin changes from yellow to greenish or greyish-blue. The prominent feature of Little Egret is its long black legs with yellow feet. Most commonly sighted in all areas of DAE Kalpakkam complex.

Published by Planning & Human Resource Management Division, SQRMG, IGCAR, Kalpakkam-603102